

RICE UNIVERSITY

Phase modulation in super-resolution microscopy

by

Wenxiao Wang

A THESIS SUBMITTED
IN PARTIAL FULFILLMENT OF THE
REQUIREMENTS FOR THE DEGREE

Doctor of Philosophy


APPROVED, THESIS COMMITTEE



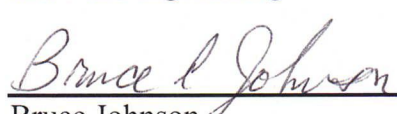
Christy F. Landes, Chair
Professor of Chemistry, Electrical and
Computer Engineering



Ashok Veeraraghavan
Associate Professor of Electrical and
Computer Engineering



Hanyu Zhu
Assistant Professor of Materials Science
and Nanoengineering



Bruce Johnson
Research Professor of Chemistry

HOUSTON, TEXAS
December 2018

ABSTRACT

Phase modulation in super-resolution microscopy

by

Wenxiao Wang

Phase modulation attracts arising attention in super-resolution studies because of the convenience and efficiency in encoding the information. Current super-resolution microscopy typically achieves high spatial resolution, but the temporal resolution remains low and obstructs most physical and chemical studies. Based on phase modulation, the novel technique Super Temporal-Resolved Microscopy is proposed to compress time information and thus improve the temporal resolution of 2D super-resolution microscopy. The fundamental basis for STReM is the utilization of a double helix phase mask that is rotated at fast speed to encode temporal information in the Fourier domain. Complicated movement can be also decomposed and reconstructed through an L_1 norm constrained optimization process. STReM has been verified using both simulated and experimental 2D data and the temporal resolution is improved 20 times when comparing traditional methods to that of the novel method of STReM presented in this thesis.

Besides the application to boost the temporal resolution, phase modulation is also applied to extract depth information in super-resolution microscopy. Most physical and chemical processes occur in 3D space and the underlying mechanism is usually unavailable or misleading due to the poor depth detection ability. Recently,

phase modulation is reported as a promising solution to 3D imaging in super-resolution microscopy. Various functions have been achieved through phase modulation such as improving the axial spatial localization precision and expanding the axial detection range. However, a current challenge is the lack of a robust and efficient algorithm to design a phase mask for arbitrary desired point spread function patterns in 3D continuous space. In this thesis the phase mask design algorithm is proposed using a phase retrieval scheme. Multiple algorithms were studied and compared for solving the phase retrieval, including Gerchberg Saxton, stochastic gradient decent, and Gauss-Newton methods. The Gauss-Newton method is proved to be the best by reaching the minima of the phase retrieval optimization. Several phase mask patterns for 3D super-resolution microscopy are proposed, and their corresponding PM patterns are successfully designed and experimentally fabricated with light lithography. Finally, by combining depth and time modulations, phase modulation is proposed to encode the information simultaneously in 4D space, which will definitely benefit super-resolution studies in the future.

Acknowledgments

I would like to express my sincere gratitude to all the people that helped, encouraged, supported, and instructed me during my five and a half years of my PhD studies.

First of all, I would like to thank my PhD supervisor, Prof. Christy Landes, for the continuous support, patience, inspiration, and immense knowledge over the course of all of my projects. Prof. Landes was not only a good instructor with my projects, but also a supervisor that will have great influence on my life moving forward. I could not imagine a better mentor for my PhD studies.

In addition to my advisor, I would like to thank the rest of my thesis committee members: Prof. Ashok Veeraraghavan, Prof. Hanyu Zhu, and Prof. Bruce Johnson, for their insightful discussions, comments, and encouragements. Your suggestions and instructions have played a critical role in all my PhD projects.

I am also very grateful to all the Landes and Link group members, for all the help and support during my studies. I want to add a special thanks to Prof. Hao Shen, Dr. Bo Shuang, and Nicholas Moringo for your professional and valuable suggestions with my research.

Last but not least, I would like to thank my family for the priceless support, trust, and encouragement.

Contents

Acknowledgments	iii
Contents.....	iv
List of Figures	vii
List of Equations	xiii
Nomenclature	xv
Introduction.....	16
1.1. Background	16
1.2. Super-resolution microscopy	18
1.2.1. Deterministic super-resolution microscopy.....	19
1.2.2. Stochastic super-resolution microscopy.....	20
1.2.3. 3D super-resolution microscopy techniques	20
1.3. Phase modulation to encode depth information	23
1.4. Low temporal resolution in super-resolution microscopy.....	24
1.5. Compressive sensing to encode temporal information.....	25
1.6. Overview.....	26
Super Temporal-Resolved Microscopy (STReM)	28
2.1. Abstract.....	28
2.2. Introduction	29
2.3. Experimental setup	31
2.3.1. Optical setup and samples	31
2.4. Results and discussion	32
2.5. Error Analyses.....	41
2.5.1. Simulations for fast adsorption/desorption and 2D transport.....	41
2.5.2. Application of Compressive Sensing to super-resolution localization.....	42
2.5.3. Alternating direction method of multipliers (ADMM) algorithm.....	43
2.5.4. The inapplicability of traditional video Compressive Sensing to super-resolution microscopy.....	45
2.5.5. Definition of temporal resolution in STReM.....	46
2.5.6. The temporal resolution limit of STReM.....	49

2.5.7. Arc-shaped PSF analysis.....	52
2.5.8. L_2 norm constraint.....	54
2.6. Conclusion.....	56
Super-temporal resolved microscopy reveals multistep desorption kinetics of α-lactalbumin from nylon	57
3.1. Abstract.....	57
3.2. Introduction	58
3.3. Materials and methods.....	60
3.3.1. α -LA labeling	60
3.3.2. Nylon 6,6 film preparation	60
3.3.3. Single molecule STReM measurements.....	61
3.3.4. Circular Dichroism Spectroscopy.....	61
3.3.5. Scanning electron microscope (SEM) imaging	62
3.3.6. Drifting α -LA events on nylon 6,6 film.....	62
3.4. Results and discussion	66
3.5. Conclusion.....	75
A generalized method to design phase masks for 4D super-resolution microscopy	77
4.1. Abstract.....	77
4.2. Introduction	78
4.3. Methods	80
4.3.1. Phase retrieval.....	80
4.3.2. Converting phase retrieval to a standard optimization problem.....	83
4.3.3. SGD optimization.....	85
4.3.4. Gauss-Newton optimization.....	86
4.3.5. Fabrication of PM using reaction-ion etching (RIE)	88
4.3.6. Commercial sourcing of optimized PM	88
4.3.7. Depth measurement and calibration.....	89
4.4. Results and discussion	89
4.4.1. Recovering well-established PMs	89
4.4.2. Stretching-lobe PSF to obtain both time and depth information in high resolution	92

4.4.3. Developing complicated PSFs.....	97
4.5. Conclusion.....	98
Conclusions	99
5.1. Summary	99
5.2. Future development.....	100
References	102

List of Figures

Figure 2.1 – Experimental setup of STReM. The sample is excited in TIRF mode with a 532 nm laser. A phase mask is installed on a rotary mount in the 4f system to modulate the phase in the Fourier domain. The sample is finally imaged at the 2nd image plane. 32

Figure 2.2. STReM is demonstrated for reversible adsorption. (a) Cartoon of imaging reversible adsorption of fluorescent emitters. (b) A DH PSF is observed with a static DHPM in the Fourier plane and the camera at the 2nd image plane. (c) The PSF orientation changes when the DHPM is rotated. (d, e) Simulated frames of reversible adsorption imaged with a static vs. a rotating DHPM, respectively. The image pixel size is 172 nm; the camera exposure time is 100 ms; the residence time of all emitters ranges from 0.5 ms to 1 ms. The DHPM is rotated at 300 rpm. The crosses denote the lateral positions of the emitters and the color denotes arrival time. (f, g) Experimental frames of orange bead reversible adsorption on glass, collected with a static DHPM and rotating DHPM (Supplementary Videos 2 and 3) respectively. Laser power is 0.52 KW/cm². The camera exposure time is 5 ms in (f) and 100 ms in (g), with DHPM rotation at 300 rpm in (g). Scale bar = 1 μ m. 34

Figure 2.3: Imaging Alexa 546 labeled α -lactalbumin (Supplementary Information) adsorption on SiO₂ surface. (a) Cartoon of α -lactalbumin adsorption on a glass coverslip. (b) Single frame image of a single adsorbed α -lactalbumin protein with 100 ms exposure time in standard collection geometry. (c) Single frame STReM image of an adsorbed α -lactalbumin molecule with rotating DHPM. The camera exposure time is 100 ms and the rotational frequency of the DHPM is 300 rpm. The red cross marks the central position of the 2D Gaussian fit for this molecule. Extracted surface residence time in (c) is 55 ± 10 ms (Supplementary Information). Scale bar = 1 μ m. (d, e) Surface residence time distribution of α -lactalbumin on glass without (d) and with STReM. (e) The red curve in (d) is fit to a single exponential and the average surface residence time is 0.2 ± 0.1 s. The red curve in (e) is fit with a single exponential rise and a single exponential decay. The fitted rise time constant is 0.04 ± 0.01 s while the decay time constant is 0.28 ± 0.01 s. 35

Figure 2.4: STReM resolves fast 2D transport by combining with an ADMM recovery algorithm. (a) Cartoon showing the simulation trajectory. A fluorescent emitter is simulated moving in a cosine wave constrained to the

2D plane of the surface (to simulate observation on a TIRF microscope). (b, c) Simulated and experimental frames of 2D transport without a DHPM. The ground truth time-resolved trajectory is plotted in (b) and the recovered trajectory is plotted in (c). (d, e) Simulated and experimental frames of 2D transport with a static DHPM. The crosses denote the recovered super-resolved 2D spatial positions. (f, g) Simulated and experimental frames of 2D transport with a rotating DHPM. The trajectory is plotted by connecting each recovered position adjacent in time. The real movements in (b, d, and f) are the same. In (c, e, and g) the sample motions are made by lateral translations of a fluorescent bead on a glass cover slip, with variable translation direction and speed. The camera exposure time is 100 ms. (h, i) Recovered trajectories of 2D transport with L_2 norm constraint for both simulated and experimental data. Note lack of sparseness in recovered data using L_2 norm constraints. Scale bar = 1 μm38

Figure 2.5 The fitting errors of fast adsorption/desorption experiments and motion-blurred trajectories with ADMM algorithm from 1000 Monte Carlo simulations. The standard deviation of the error distribution in time for single DH PSF fitting (a) and ADMM (b) are ~ 2.0 ms and ~ 2.4 ms respectively. The spatial error with ADMM is shown in (c) with the standard deviation being 65 nm.....47

Figure 2.6 Systemic error analysis. (a) The cumulative distribution functions (CDF) of DH PSF orientation from 1000 experimental frames with static phase mask and fitting curve with exponential decay model. The $1/e$ error is ~ 8 degrees out of 180 degrees, corresponding to the intrinsic error of STReM, $\sim 5\%$ of the camera exposure time. (b) The probability density function (PDF) of the same events in (a). The red curve fits the PSF orientation distribution with an exponential decay model.....49

Figure 2.7 Temporal resolution of STReM for emitters with different SNR and moving velocities, and varying rotational speed of the DHPM calculated by Monte Carlo simulations. (a) The fitting error from simulated fast adsorption/desorption experiments. (b) The fitting error from simulated 2D transport experiments with ADMM recovery algorithm. The red dashed line indicates a cutoff for the fitting algorithm. (c) The temporal resolution of STReM for emitters of different translational velocities. The red line indicates a cutoff for the STReM for the simulated emitter. The cutoff can be pushed towards a higher moving speed with a brighter dye molecule. (d) The temporal resolution of STReM for different rotation speed of DHPM. The

rotation speed was normalized by 300 rpm. The camera exposure time in (a) – (d) was 100 ms. 50

Figure 2.8 The fitting of arc-shaped PSFs and error analysis. (a) Raw experimental data of α -lactalbumin adsorbed on clean coverslip. (b) The length fitting of arc-shaped PSF. Scale bar = 1 μ m. (c) The objective function value in a 2D map with different starting and ending orientations of the arc. Highest value of the objective function corresponds to orientation of separating two arcs. (d) Fitting error in time of arc-shaped PSF from 1000 Monte Carlo simulations. The standard deviation error of fitting the arc-shaped PSF is ~9.4 ms out of 100 ms exposure time. 54

Figure 2.9 Recovered results of simulated 2D motion blurred trajectories with L_2 norm constraint. (a) The recovery results of 2D motion blurred trajectories with L_2 norm constrained optimization. The results of L_2 norm optimization contain numerous artifacts, as expected. (b) Recovered time trajectory by connecting points adjacent in time. (c) Incorrect wobbling trajectory generated from L_2 norm minimization from the highlighted region in b. Scale bar = 1 μ m. 56

Figure 3.1. Different possible adsorption behaviors in simulations and experiments. (A) Simulated (first row) and experimental PSFs (second row) of adsorbed α -LAs that adsorb on the interface for shorter than 1 frame, longer than 1 frame, and drift. (B) Percentage of drifting events, adsorption events that last for less than 1 camera frame, and adsorption events that last for longer than 1 camera frame. 63

Figure 3.2. Simulated distorted STReM PSFs. (A-C) of slow in plane emitter diffusion in different directions indicated with red arrows. Insets (A-C) within each figure are the same simulated PSF taken with a traditional microscope. 64

Figure 3.3. Distorted PSF identification via intensity thresholding. (A) The PSF of an immobile adsorption event lasting for less than 1 frame and the resulting (B) binary image after the intensity threshold. The red circle in B is used to count the number of gaps in the resulting PSF, with the centroid shown with the red crosshair. (C) PSF of event that lasts for more than 1 frame and the resulting (D) binary image. No gaps are found in this PSF. (E) Distorted PSF caused by drifting and (F) binary image showing only one gap in the resulting PSF. Scale bar = 1 μ m. 65

Figure 3.4 - Accuracy and misclassification rate in detecting distorted PSFs using different intensity thresholds.....66

Figure 3.5. Experimental setup of STReM and simulated PSFs in STReM. (A) STReM experimental setup. Fluorescently tagged α -LA proteins at the water-polymer interface are excited with a total-internal-reflection geometry. Fluorescence is transferred into the Fourier domain after the 1st image plane and sub-frame dynamics are encoded in the resulting PSFs by a rotating phase mask [24, 25]. The final image is captured by a sCMOS at the 2nd image plane. (B - E) Simulated PSFs observed in STReM. (B) The angle of the PSF reflects the arrival time; (C) the arc length encodes the dwell time for events shorter than one frame versus (D) longer than one frame. 95% of almost 16,000 α -LA adsorption events were classified under these two types of adsorption/desorption. (E) Simulated PSF for 2D motion, exhibited by 5% of α -LA adsorption events. The insets in (C - E) denote their percent contribution in experiments and scale bar = 1 μ m.67

Figure 3.6. Kinetic analysis of α -LA adsorption on nylon 6,6 film with STReM. (A) Representative STReM single frame containing sub-frame (blue and green) and longer (red) protein adsorption events. (B - D) Zoomed PSFs in (A). The surface residence time (SRT) is determined from the arc length of the PSF shown with the blue arrows in (B), and (C). The green arrows denote one camera exposure of 100 ms. For events longer than one frame such as (D), the SRT is determined by cumulating its PSF arc lengths in all consecutive frames. (E, F) The probability distribution function (PDF) of SRT for adsorbing α -LA on thin nylon 6,6 film without (E) and with STReM (F). The data in (E) is fit with a single exponential decay function, while the data in (F) can only be fit with a two-term exponential function. Scale bar is 5 μ m in (A) and 1 μ m in (B-D).70

Figure 3.7. α -LA desorption and structural changes in the presence of sodium chloride. (A) SRT distributions for single α -LA molecules under various sodium chloride concentrations. Blue curves are fit using Eq. 4. (B) The fitted rate constants are plotted versus different sodium chloride concentrations. (C) Circular dichroism measurements of α -LA in various experimental conditions. Error bars in (A) and (B) are standard deviations from three different trials containing 8,000 frames respectively. (D) Cartoon depicting the proposed desorption mechanism. The black lines indicate the interaction between proteins and the nylon surface.74

Figure 4.1. Layout of a typical PM based 3D super-resolution microscope. The 4f system is shown in the red box consisting of two lenses and a PM at the

Fourier plane. Emission light is modulated by the 4f system and projected to a camera..... 82

Figure 4.2. Fabrication process of the PM using photolithography. A total of nine iterations are involved with each using a different photomask. Patterns are etched to the substrates after photoresists are developed in each iteration of photolithography. Scale bar = 100 μm in SEM image. 88

Figure 4.3. PM fabricated using RIE and corresponding DH PSFs. (A) Initial guess for the PM pattern. (B) Intensity profiles of the desired PSFs. These intensity profiles are used as the input for the PM design. Each PSF contains two Gaussian distributed lobes and the orientation varies at different depth. The white crosses denote the center position of the lobes, which is the lateral position of the emitter in 3D super-resolution microscopy. (C, D) The recovered PM (C) and its corresponding PSFs at different depths (D). (E, F) The fabricated PM (E) and the measured PSFs at different depths (F). The scale bar in A, C, and E is 500 μm and 1 μm in B, D, and F..... 91

Figure 4.4. PM fabricated using RIE and corresponding stretching-lobe PSFs. (A) Initial guess for the PM pattern. (B) Intensity profiles of the desired PSF. Each PSF contains two Gaussian distributed lobes and the distance between two lobes varies at different depth. The white crosses denote the center position of the lobes, which is usually the lateral position of the emitter in 3D super-resolution microscopy. (C, D) The recovered PM (C) and its corresponding PSFs at different depths (D). (E, F) The fabricated PM (E) and the measured PSFs at different depths (F). The scale bar in A, C, and E is 500 μm and 1 μm in B, D, and F..... 93

Figure 4.5. Scanning electron microscope (SEM) image of two regions on stretching-lobe PM. Different depths of the surface feature is achieved by multiple layer light-lithography. 94

Figure 4.6. Localization precision of stretching-lobe PSFs. Localization precision in both lateral and depth directions predicted by 1,000 Monte Carlo simulations per data point..... 95

Figure 4.7. Experimental PSFs of stationary green beads when rotating the stretching-lobe PM fabricated using gray-scale lithography. PSFs of different orientations (rows) denote different time; PSFs of different lobe distance (columns) denote different depth of the emitter. The scale bar is 1 μm 96

Figure 4.8 PM fabricated using RIE for complicated PSFs. (A) Initial guess for the PM pattern. (B) Intensity profiles of the desired PSF. Four letters at different depths serve as four constraints. (C, D) The recovered PM (C) and its corresponding PSFs at different depths (D). (E, F) The fabricated PM (E) and the measured PSFs at different depths (F). The scale bar is 500 μm in A, C, and E, while it equals to 1 μm in B, D, and F. 98

List of Equations

Equation 2.1 – domain transformation	42
Equation 2.2 – L_1 norm constrained problem	43
Equation 2.3 – Image convolution with kernels.....	44
Equation 2.4 – L_2 norm constrained problem	44
Equation 2.5 – Augmented Lagrangian. λ , μ and ν are relaxation parameters and we use $\lambda = 0.005$, $\mu = 1$, and $\nu = 20$; η_0 , η_1 , u_0 and u_1 represent the simplified optimization problem of solving x from Equation (4.4).	45
Equation 2.6 – Spatial resolution and photon number.....	46
Equation 2.7 – Best time resolution in STReM.....	46
Equation 2.8 – Fitting error of time in STReM	46
Equation 2.9 – Coherence between two matrices.....	52
Equation 2.10 – Single metric for arc separation.....	52
Equation 3.1 – Surface residence time calculation.....	67
Equation 3.2 – Simple adsorption/desorption model.....	69
Equation 3.3 – Residence time distribution	69
Equation 3.4 – Residence time distribution of proposed model	72
Equation 4.1 – Relationship between phase mask and PSF	81
Equation 4.2 – Phase mask design equation.....	82
Equation 4.3 – Residual function	83
Equation 4.4 – Objective loss function.....	83
Equation 4.5 – Phase mask calculation	84
Equation 4.6 – Fourier transform represented by matrix multiplication	84

Equation 4.7 – Fourier transform operation matrix.....	84
Equation 4.8 – Re-formatting the phase mask design problem.....	85
Equation 4.9 – Jacobian matrix	86
Equation 4.10 – Gradient of objective function	87

Nomenclature

PSF	Point Spread Function
PM	Phase Mask
2D	Two-dimensional
3D	Three-dimensional
STED	Stimulated Emission Depletion
STROM	Stochastic Optical Reconstruction Microscopy
PALM	Photo-activated localization microscopy
fPALM	fluorescence Photo Activation Localization
Microscopy	
DMD	Digital Mirror Device
SLM	Spatial Light Modulator
SNR	Signal to noise ratio
ADMM	Alternating Direction of Method of Multipliers
STReM	Super-Temporal Resolved Microscopy
DH	Double Helix
DHPM	Double Helix Phase Mask
TIRF	Total Internal Reflectance Fluorescence
CDF	Cumulative distribution function

Chapter 1

Introduction

1.1. Background

Scientists spared no effort to push the limit of light microscopy in order to understand the nanoscale world. The first light microscope was invented by Robert Hooke [1]. Afterwards Antony van Leeuwenhoek improved the spatial resolution of existing microscopes by two times by crafting high quality lenses, thereby enabling the observation of individual cells, such as bacteria, muscle cells, and sperm [2]. In the nineteenth century the light microscope was largely improved by Carl Zeiss and Ernst Abbe who developed superior lenses that suppressed chromatic and spherical aberrations. The spatial resolution was largely improved by these advances, and magnification capabilities were improved as well [3]. The fundamental working principle of light microscopy is to use photons as a probe to image objects much

smaller than human eyes resolution limit. This principle also serves as the guideline for the other form of microscopy.

As the object size decreases and becomes comparable to the probes wavelength, the spatial resolution of the microscope can be hardly improved, as defined by Ernst Abbe [4-6]. To further improve the spatial resolution, it is straightforward to apply probes of even smaller size than visible light [7, 8]. Ultraviolet microscopy was also invented to achieve a higher spatial resolution because of its shorter excitation wavelength compared to visible light. However this improvement is still a refinement based on the current spatial resolution, and objects smaller than ~ 100 nm are not detectable. This fundamental resolution limit constricts the ability to observe and study behaviors of single molecules and macromolecules at the nanoscale. A revolutionary breakthrough was made to microscopy theory at the beginning of the 20th century when the wave-particle duality was proposed by Huygens and Fresnel [9]. Electron beams exhibit wave-particle duality character and can be used as an imaging source to study nanoscale topologies [10, 11]. An electron's wavelength is roughly 100,000 times shorter than visible light, resulting in much higher imaging resolution [12].

The use of high energy imaging sources, such as electron beams, introduces a challenge to the types of systems that can be imaged since these sources have much higher powers and can damage delicate samples [13]. Inorganic materials, such as metal, are not structurally affected by the electron beams. However most functional surfaces composed of organic and biological materials are easily affected or

destroyed after interacting with electron beams [13]. Additionally, the high power makes it difficult to repeat experimental observations, which largely obstructs the reproducibility of observables in most chemical and biological studies. Light microscopy overcomes this challenge by limiting damage to complex systems such as chemical and biological materials, but the spatial resolution needs to be improved to provide details about fundamental studies at the nanoscale, such as understanding cell structures and intracellular interactions.

1.2. Super-resolution microscopy

Super-resolution microscopy was proposed at the beginning of the 21st century by employing implicit information encoded by probes when interacting with features of smaller size than the probe [4-6, 14, 15]. Generally, the spatial resolution of a light microscope is roughly half of the excitation wavelength, which is also known as the Abbe diffraction limit [4-6]. For a single emitter, the photons in the image plane spread as a Gaussian distribution instead of focusing at a single point. The distribution of a point source is called the point spread function of a microscope system, and the standard deviation of the PSF is a good metric to directly measure the uncertainty of single emitter position, which is also the spatial resolution. The photons do not explicitly locate the spatial position of an emitter, but instead following a certain distribution around the center position. Despite the uncertainty of the photon distribution, the true position estimate of the single emitter can be refined within 20 nm for visible light source by statistically

maximizing the maximum likelihood estimator of the photon distribution [6]. However, it should be noted that the 20 nm spatial resolution is only restricted to the scenario of a single emitter that is sparse in space. In most cases, crowding between multiple molecules is of realistic concern to scientists. For example, two emitters cannot be distinguished when they are close to each other within the Abbe diffraction limit [16]. From this perspective, the problem of low resolution in light microscopy is not solved yet, and becomes the target problem in super-resolution microscopy.

1.2.1. Deterministic super-resolution microscopy

The first type of super-resolution microscopy is STED microscopy which is a deterministic microscopy technique [14, 15]. As discussed above, the photons are dispersed on a detector roughly following a Gaussian distribution. The standard deviation of the resulting PSF is the metric to measure the spatial resolution. Therefore the spatial resolution can be improved by shrinking the size of the PSF, which is exactly what STED microscopy achieved. In a standard STED microscope, two laser beams are applied to illuminate the fluorescent emitters. On one hand, the excitation laser beam excites the fluorescent emitter and forms a PSF of Gaussian distribution within the diffraction limit. On the other hand, an additional quenching donut shaped laser beam turns off the fluorescent signal within its illumination area. Combining the effects of the two laser beams, the effective PSF of the single emitter of interest has a much smaller standard deviation, which increases the overall spatial resolution below the diffraction limit posed by Abbe. This process is carried

out iteratively over the surface of a sample to build a super resolution image. STED microscopy has benefitted multiple biomedical and chemical studies [14, 17].

1.2.2. Stochastic super-resolution microscopy

In comparison to deterministic microscopy in which the PSF is directly modified, stochastic super-resolution microscopy achieves high spatial resolution by sparsely exciting and localizing fluorescent emitters [4-6]. Two emitters within the diffraction limit cannot be distinguished when excited simultaneously, however they can be localized individually with high resolution if each emitter is excited separately in time. Representative stochastic super-resolution microscopy includes STORM [6], PALM [4], and fPALM [5]. Usually all the photo-switchable fluorophores are put in an 'off' state by applying the first laser beam. Then the excitation laser beam stochastically excites a sparse subset of emitters. The density of excited emitters is low enough to guarantee that PSFs do not spatially overlap with each other, enabling the fitting of single PSFs and thereby building up a high spatial resolution image. By repeating this process thousands of times, which benefits from the advancements of photo stable and switchable fluorophores [18-20], the target structure can be reconstructed with a high spatial resolution, usually around ~ 20 nm. This spatial resolution is roughly 10 times better than the Abbe diffraction limit.

1.2.3. 3D super-resolution microscopy techniques

Super-resolution microscopies have also pushed the frontier of resolution in depth in addition to lateral resolution discussed above. Existing 2D super-resolution

microscopies, such as 2D STORM, PALM, and fPALM, capture only a slice of an image from 3D sample space. However physical and chemical processes in many domains of science occur in 3D space and can be fully understood and explained only if 3D information is collected [21]. There is not a camera that is able to capture three-dimensional images simultaneously in one shot. As a result, the first challenge is to encode and record 3D information using a 2D data collection method. The data collection during this process must be fast in order to preserve the time resolution of the data. The depth information should be transferred and compressed into 2D images, and the compression should be reversible and not decrease the lateral spatial resolution. Secondly the depth information is usually encoded and will be extracted by combining additional information in consecutive 2D frames, which leads to a low fault tolerance because the low quality of one 2D image would possibly make the whole 3D reconstruction highly difficult and misleading. Finally, advanced data analyses methods are necessary to recover 3D information from 2D, which is usually an over-constrained optimization problem. To summarize, evolving from 2D to 3D microscopy requires rigorous experimental design, fast data acquisition, and precise data analysis methods. All 3D microscopy techniques are designed following these three principles.

Multiple depth reconstruction methods were proposed in super-resolution microscopy but have different performances as to complexity of the system design, data collection, spatial resolution in 3D, and depth detection range. Modern 3D super-resolution microscopies include but are not limited to multifocal plane

microscopy [22], astigmatic 3D detection using cylindrical lenses [23], and engineered PSFs using phase modulation [24]. Multifocal plane microscopy was developed by Raimund J. Ober and his co-workers. In this technique, multiple cameras are located at different focal planes so that the ensemble of multiple 2D images reconstructs the 3D spatial information. It is also necessary to calibrate the system between the focal planes in sample space and image space prior to data collection, which leads to a large complexity of the imaging system. Astigmatic 3D detection achieves depth detection with a relative convenient method by inserting a cylindrical lens in the light path after the tube lens, and encoding the depth information into single 2D image. The cylindrical lens breaks the symmetry of the imaging system, and the original Gaussian PSF becomes an elliptical Gaussian PSF, with the ratio between two axes encoding the depth of the emitter. The typical depth localization resolution could be ~ 40 nm with visible excitation light, while the drawback is that the detection range is small, usually restricted to $1\text{ }\mu\text{m}$. 3D microscopy using phase modulation encodes depth information via PSF engineering methods. A representative phase modulation pattern was proposed and demonstrated in 2008 by Rafael Piestun at the University of Colorado Boulder [25]. Similar to astigmatic 3D detection, the shape of the PSF was modified and encoded with depth information of the emitter. Benefitting from a direct modulation on the phase information, the signal response to the emitter depth can be various and customized based on the need. Compared with the previous two techniques, this method is relatively simple as to the system complexity and has a large depth

detection range, usually several micrometers. Thus this technique will be the focus in this thesis.

1.3. Phase modulation to encode depth information

Fourier optics is the basis to understand how the depth information is encoded in the PSFs [26]. The Fourier transform can mathematically explain the process of a collimated light being focused at the focal plane after a lens. Light signal is focused at the focal plane and belongs to the spatial domain. The signal is decomposed into components of different frequency when transferred into the Fourier domain. Ideally the lens is infinitely large so that all frequency components would be collected and the signal would be reconstructed perfectly in the spatial domain. However, the lens usually has limited size and cuts off high frequency components, represented as a sampling function (Sinc function). The Fourier transform of such a signal leads to a spread of the sampling function instead of a delta function, of which the intensity is also known as the Airy disk. The Airy disk is usually fitted by a Gaussian distribution and the width is inversely related to the input dimension of the sampling function. The missing components of specific frequencies in the transmission are the direct cause of the diffraction limit, and any PSF response is determined by both the incident light and the optics composing the lightpath. Thus, to encode the depth information into PSFs, modifications should be made between sample space and detection space.

3D super-resolution microscopy using phase modulation essentially modifies the microscope response to depth by modifying the detection path. Existing 2D super-resolution microscopy has specific responses to emitters depth change, expanding in width as the emitters depth changes. Unfortunately this response encodes little depth information because the standard Gaussian PSFs spread quickly as the emitters go deeper, and the peak intensity drops dramatically so that it is easily submerged by noise and encodes little depth information [26]. Furthermore, when the emitter moves in the opposite direction by the same distance, the PSF values are theoretically identical, requiring the further complication that depth information is determined from a symmetric PSF response. To conclude, the microscopy response must be modified to generate a PSF that is able to uniquely encode depth information. Furthermore, to increase the SNR of the image, this modification should be direct modification of the phase of light instead of the amplitude. Amplitude modification is not ideal since the number of photons collected should not be lost in order to perform super-resolution microscopy which is highly dependent on photon budgets. Multiple phase modulation patterns and relevant applications will be discussed in this thesis in Chapter IV.

1.4. Low temporal resolution in super-resolution microscopy

Even though the spatial resolution has been improved rapidly in recent years, the temporal resolution in super-resolution microscopy remains slow to collect and therefore unsatisfactory in many chemical and biological studies [27].

Many chemical and biological processes happen beyond the best existing temporal resolution of the system, and the observed experimental phenomenon is the ensemble effect with slow imaging rates [28]. To fully understand the mechanism behind the ensemble effect, the ‘probe’ should be smaller in the ‘time dimension’, which is the same with increasing spatial resolution. The temporal resolution of scientific detectors has a limitation, which introduces the tradeoff between the frame rate and overall SNR of an image. Similar to encoding the depth information, the temporal information can be also treated as an additional dimension and therefore be encoded and compressed into a slower device. Furthermore, this compression should be reversible, and guarantee the successful reconstruction with little information loss.

1.5. Compressive sensing to encode temporal information

Compressive sensing is a powerful data compression tool that is able to reconstruct the original signal with high precision and little information loss. As a result, it is a good candidate to encode the temporal information in super-resolution microscopy [29, 30]. Compressive sensing encodes the information with two steps, compressively sensing and decoding. It should be noted that the high resolution information is encoded during or prior to the data collection. An encoder with good dynamical properties is usually inserted in the detection path, such as in a DMD or a SLM. The temporal resolution of those encoder devices must be faster than the camera, and the final temporal resolution to be recovered would be no better than

that of the encoder [30]. Another important task for the encoder is to add some specific transformation to the high temporal resolution information. This is an important step because direct accumulation of time stream data will lead to the loss of the temporal information generated by encoder.

Sparsity is an important hypothesis to guarantee successful decoding in compressive sensing. Sparsity means most of the entries are zero or relatively small compared with non-zero entries. The sparsity hypothesis in compressive sensing is made directly to the original signal or the signal after some transformation, such as the wavelet transform or Fourier transform. Sparsity introduces an additional constraint in the optimization, the L1 norm constraint. Combined with the L1 norm constraint, the signal with high temporal resolution can be reconstructed. It should be highlighted that the signal is directly encoded and modified in the Fourier domain instead of the spatial domain in this thesis, which is one of the major contributions of this work to super-resolution or compressive sensing studies.

1.6. Overview

The overall contribution of this thesis is the discussion of the application of phase modulation to super-resolution microscopy. In Chapter II, the Fourier domain and 4f system basis are discussed and the notion of STReM is proposed. The information of high temporal resolution is encoded in the Fourier domain and compressed in the spatial domain. By employing an ADMM algorithm to analyze the compressed data, the final temporal resolution of the imaging system is improved

20 times compared with the native camera frame rate. In Chapter III, fast adsorption and desorption of α -lactalbumin on the Nylon 6,6 surface are studied using the proposed STReM system. A brand new desorption pathway is observed by collecting data with a high temporal resolution, STReM, in comparison to traditional microscopy techniques. In Chapter IV, a robust and generalized phase mask design method is proposed for encoding additional information on 2D images. Multiple phase mask patterns are proposed and demonstrated in both simulation and experiment to encode depth information from 2D images. Finally, future development of phase modulation is discussed in Chapter V. By combining the phase modulation in both depth and time, it is possible to simultaneously obtain 4D information of high resolution, which will definitely benefit single molecule and super-resolution studies in the future.

Chapter 2

Super Temporal-Resolved Microscopy (STReM)

2.1. Abstract

Super-resolution microscopy typically achieves high spatial resolution but the temporal resolution remains low. We report STReM to improve the temporal resolution of 2D super-resolution microscopy by a factor of 20 compared to the traditional camera-limited frame rate. This is achieved by rotating a phase mask in the Fourier plane during data acquisition and then recovering the temporal information by fitting the PSF orientations. The feasibility of this technique is verified with both simulated and experimental 2D adsorption/desorption and 2D emitter transport. When STReM is applied to measure protein adsorption at a glass surface, previously unseen dynamics are revealed.

2.2. Introduction

Super-resolution fluorescence microscopy [4-6, 23, 31, 32] breaks the spatial diffraction limit at optical wavelengths, but the temporal resolution remains low compared to the timescale of many scientifically relevant processes [27, 33]. A typical spatial resolution of ~ 20 nm can be obtained by exciting a fractional subset of fluorescent emitters and localizing isolated PSFs [4-6]. However the temporal resolution is limited by the frame rate of the detector array. Dynamical processes occurring faster than the frame rate are integrated into the same exposure time window and thus appear identical in time. The temporal resolution thus limits the application of super-resolution microscopy to processes occurring at or slower than the acquisition time of a single frame [27].

Several approaches have been applied to capture fast events, including better sCMOS chips[34] and streak cameras [35], but these are either limited in temporal improvements or prohibitively expensive. New techniques in data compression and reconstruction such as compressive sensing [36-41] have also been proposed to improve both spatial and temporal resolution. However, in many of the current video compressive sensing techniques, a spatial light modulator (such as digital micromirror device [35, 42-44]) is used to encode the amplitude of the signal, but decreases the number of photons reaching the detector in most situations, which sacrifices spatial resolution [22, 45, 46].

In this work, we report Super Temporal-Resolved Microscopy, STReM, to improve the temporal resolution by as much as 20 times faster than the camera

frame rate. STReM is achieved by employing a rotating DHPM. Traditionally, a static DHPM [25] is used to achieve super-resolution in 3D [47-50] wherein the depth information of each emitter is encoded in the orientation of the resulting DH PSFs. Phase mask techniques are increasingly used in imaging biological structures [51-54] and single particle tracking [55, 56] because they are relatively simple and affordable to implement and return low 3D localization uncertainty. In the current application, the DHPM is rotated with a controllable angular speed, and the resulting DH PSF orientation instead encodes the temporal information. Information of fast 2D dynamics is compressed into each camera frame at the longer integration time and then reconstructed by either single PSF fitting or ADMM recovery algorithm [29, 38, 57, 58]. As we will show, by recovering the signal using an L_1 norm constrained ADMM algorithm we recover the trajectory closer to the ground truth compared with a traditional least squares approach that produces numerous artifacts. L_1 norm constrained minimization favors a sparse result; thus, it is able to extract the correct information and depress artifacts from the background noise. In addition, only around 10% of photons are lost during the data encoding as a result of the transparency of the DHPM [59], allowing both high time resolution and high 2D spatial resolution.

2.3. Experimental setup

2.3.1. Optical setup and samples

Figure 2.1 shows the experimental setup of STReM. Carboxylate-modified polystyrene 100 nm beads (orange fluorescent, max abs/em: 540/560 nm, Invitrogen) were diluted by a factor of 1:1000 from stock concentration in HEPES buffer (GIBCO, 10 mM, PH = 7.3). The probe molecule, α -lactalbumin was labeled by the Willson group at the Department of Chemical and Biomolecular Engineering, University of Houston. Each α -lactalbumin was labeled by three Alexa 546 molecules. In the experiments the α -lactalbumin protein is diluted to 10 nM in water. Detailed labeling methods can be found in our previous publication [13]. The fluorescent samples were excited by a 532 nm laser (Coherent, Compass 315M-100SL). The fluorescent signal was collected through a 1.45 NA, 100 \times , oil-immersion objective (Carl-Zeiss, alpha Plan-Fluar) imaged by a scientific CMOS camera (Hamamatsu, ORCA- Flash 4.0). We used 2 by 2 binning of the sCMOS pixels when collecting the data. The fluorescent samples were excited with TIRF with a penetration depth of ~ 85 nm [60]. Fluorescent emitters were imaged at the intermediate image plane and then converted into the Fourier domain by a 75mm lens in a 4f configuration (Figure 2.1). The signal was then encoded in the Fourier domain with a phase mask (Double Helix LLC, Double Helix PSF phase mask) converting the PSFs to a DH shape. The two lobes of the DH PSF are very close in shape and the centers of the two lobes correspond to the lateral position of the

emitter. The phase mask was mounted on a motorized rotary mount (QIOPTIQ, Rotary Mount with Servo Motor), with the rotation speed controlled by an input DC voltage and monitored by a light reflective barrier (QIOPTIQ, Photo Sensor for Rotary Mount). The output signal was collected by an oscilloscope to measure the rotation speed. The encoded signal was then projected by a second 4f lens on a sCMOS camera (2048×2048 pixel) operated at 100 fps.

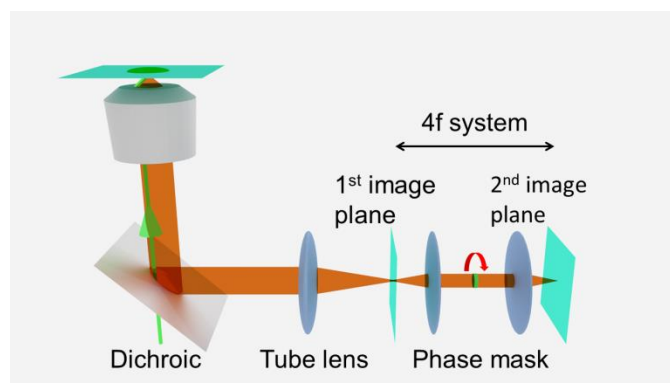


Figure 2.1 – Experimental setup of STReM. The sample is excited in TIRF mode with a 532 nm laser. A phase mask is installed on a rotary mount in the 4f system to modulate the phase in the Fourier domain. The sample is finally imaged at the 2nd image plane.

2.4. Results and discussion

By rotating the DHPM and the subsequent reconstruction, it is possible to temporally resolve processes occurring faster than the camera frame rate, such as reversible, transient adsorption of fluorescent emitters. A fluorescent emitter has a Gaussian PSF without a DHPM, which becomes a DH PSF (Figure 2.2a,b) when a

static DHPM is installed in the 4f system [61]. If the emitters stay in one plane, the orientation between the two lobes of the DH PSF will not change with a static DHPM. Meanwhile the two lobes of the PSF rotate synchronously when the DHPM is physically rotated (Figure 2.2c). To make sure that the time is uniquely labeled by the PSF orientation, the DHPM is rotated 180 degrees within one camera exposure time. In the simulated experiments with a static DHPM, multiple emitters adsorb on the object plane but at different times. The recorded DH PSFs are orientated identically (Figure 2.2d), providing similar information to Gaussian PSFs. By rotating a DHPM, all the observed PSFs still have two Gaussian lobes because only a transient moment (~ 0.5 ms out of 100 ms exposure time) is recorded, but the orientation of each PSF now expresses the arrival time (Figure 2.2e). The variation in PSF orientations recorded within one frame indicates emitters arriving at the substrate at different times. By fitting the DH PSFs with lateral positions and orientations, both spatial and temporal information are extracted.

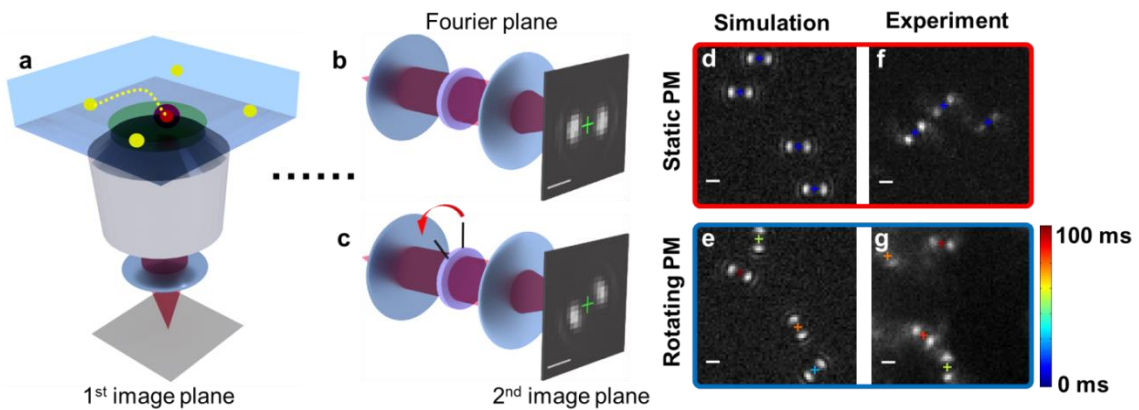


Figure 2.2. STReM is demonstrated for reversible adsorption. (a) Cartoon of imaging reversible adsorption of fluorescent emitters. (b) A DH PSF is observed with a static DHPM in the Fourier plane and the camera at the 2nd image plane. (c) The PSF orientation changes when the DHPM is rotated. (d, e) Simulated frames of reversible adsorption imaged with a static vs. a rotating DHPM, respectively. The image pixel size is 172 nm; the camera exposure time is 100 ms; the residence time of all emitters ranges from 0.5 ms to 1 ms. The DHPM is rotated at 300 rpm. The crosses denote the lateral positions of the emitters and the color denotes arrival time. (f, g) Experimental frames of orange bead reversible adsorption on glass, collected with a static DHPM and rotating DHPM (Supplementary Videos 2 and 3) respectively. Laser power is 0.52 KW/cm². The camera exposure time is 5 ms in (f) and 100 ms in (g), with DHPM rotation at 300 rpm in (g). Scale bar = 1 μ m.

STReM is also demonstrated experimentally with reversible adsorption of fluorescent beads on a glass coverslip (Figure 2.2f-g). Fluorescent beads (100 nm diameter, orange fluorescent, Invitrogen) in water are imaged in Total Internal Reflection Fluorescence (TIRF) mode so that only adsorption at the glass/water interface is observed. The raw image in Figure 2.2f was collected with a static DHPM. All of the corresponding PSFs are orientated in the same direction, which is consistent with the simulation in Figure 1d for uniplanar adsorption. In Figure 2.2g the temporal information is encoded by rotating the DHPM at 300 rpm. The recorded PSFs in Figure 2.2g are all at different orientations, denoting different arrival times during one frame. From simulated error analyses, we demonstrate a temporal resolution of ~ 5 ms for the measurement of bead adsorption dynamics with a camera exposure time of 100 ms.

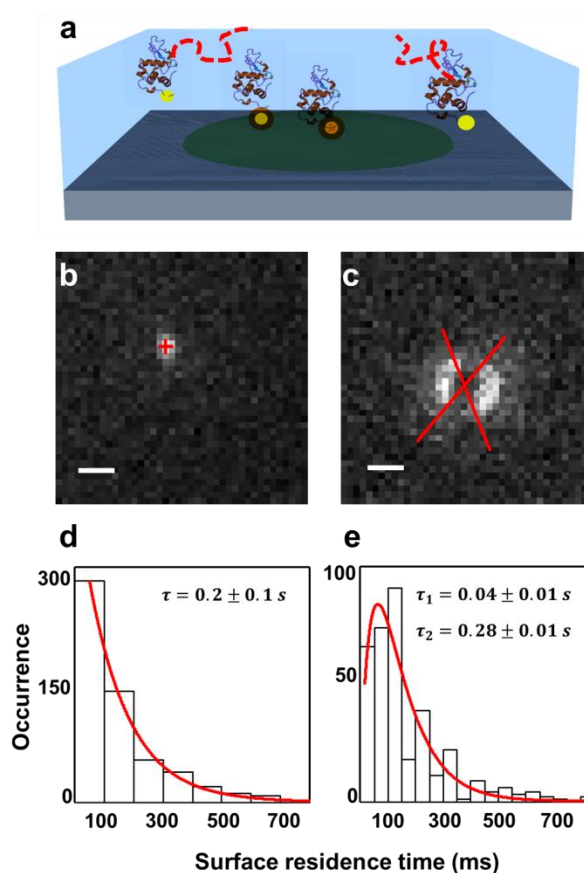


Figure 2.3: Imaging Alexa 546 labeled α -lactalbumin (Supplementary Information) adsorption on SiO_2 surface. (a) Cartoon of α -lactalbumin adsorption on a glass coverslip. (b) Single frame image of a single adsorbed α -lactalbumin protein with 100 ms exposure time in standard collection geometry. (c) Single frame STReM image of an adsorbed α -lactalbumin molecule with rotating DHPM. The camera exposure time is 100 ms and the rotational frequency of the DHPM is 300 rpm. The red cross marks the central position of the 2D Gaussian fit for this molecule. Extracted surface residence time in (c) is 55 ± 10 ms (Supplementary Information). Scale bar = $1 \mu\text{m}$. (d, e) Surface residence time distribution of α -lactalbumin on glass without (d) and with STReM. (e) The red curve in (d) is fit to a single exponential and the average surface residence time is 0.2 ± 0.1 s. The red curve in (e) is fit with a single exponential rise and a single exponential decay. The fitted rise time constant is 0.04 ± 0.01 s while the decay time constant is 0.28 ± 0.01 s.

STReM can also be used to extract surface residence times even when the adsorption rate constants are long with respect to the rotational frequency of the DHPM (Figure 2.3a), as can occur with protein adsorption to a glass coverslip. The data shown in Figure 1 occur when both adsorption and desorption occur fast in comparison to the rotational frequency of the DHPM. When slower desorption is imaged with STReM, the resulting PSFs are arc-shaped, with the arc-length related to surface residence time. In our experiments, Alexa 546 labeled α -lactalbumin was diluted to the nano-molar regime in water and was placed on a plasma-cleaned glass slide. It has been observed that protein interfacial transport is complicated and often subdiffusive due to intermittent surface interactions that depend strongly on both substrate and protein chemistry [62, 63]. For these proof-of-concept experiments the α -lactalbumin-glass interaction is chosen because it has been previously shown to be dominated by free diffusion with negligible sub-diffusion [64], in order to demonstrate the ability of STReM to quantify rare, fast adsorption/desorption events. The α -lactalbumin-glass interaction is indeed dominated by un-detectable free diffusion with only rare adsorption/desorption events. Figure 2.3b shows one frame of α -lactalbumin adsorption on a glass coverslip with 100 ms camera exposure time. The surface residence time within this frame is regarded to be 100 ms, because it is restricted by the camera exposure time. In Figure 2.3c the adsorption and desorption of α -lactalbumin proteins are imaged with STReM. The PSF with two arcs are fit [65] and the length of arcs shows that the surface residence time in the frame is 55 ± 10 ms, a higher resolution than

the camera exposure time. Because of the small size of the proteins (3 nm in diameter) [66], the effect of protein rotational motion on the signal is negligible. Moreover, the estimated diffusion coefficient of the protein in solution is $\sim 173 \mu\text{m}^2\text{s}^{-1}$ [64], therefore, fast diffusion in the bulk solution does not significantly influence the collected signal.

The ability to quantify a broad range of adsorption and desorption rate constants is important to multiple applications [13, 67-70]. For example, reversible adsorption/desorption of proteins at interfaces is crucial to protein separations [71, 72]. Recent work by our group and others has shown the promise of applying single molecule methods to link mechanistic detail about protein adsorptions to macroscale separations [13, 73-76]. However, the Schwartz group has pointed out that one barrier to broad application of this link is the inability to measure adsorption dynamics faster than traditional camera frame times [28]. The adsorption kinetics of α -lactalbumin on a glass slide are compared without and with STReM (Figure 2.3d, e). The adsorption dynamics were first determined using published 2D event analysis algorithms [77]. As shown in Figure 2.3d, the surface residence time distribution follows a single exponential decay, with decay time constant $\tau = 0.2 \pm 0.1$ s. Such a decay supports that desorption of α -lactalbumin follows first order kinetics. However, upon the application of STReM (Figure 2.3e), the higher temporal resolution reveals more complex dynamics that exhibit a rise-and-then-decay behavior. Although such a mechanistic examination is beyond the

scope of this communication, our preliminary findings clearly demonstrate that STReM makes it possible to mine a range of interfacial processes for new details.

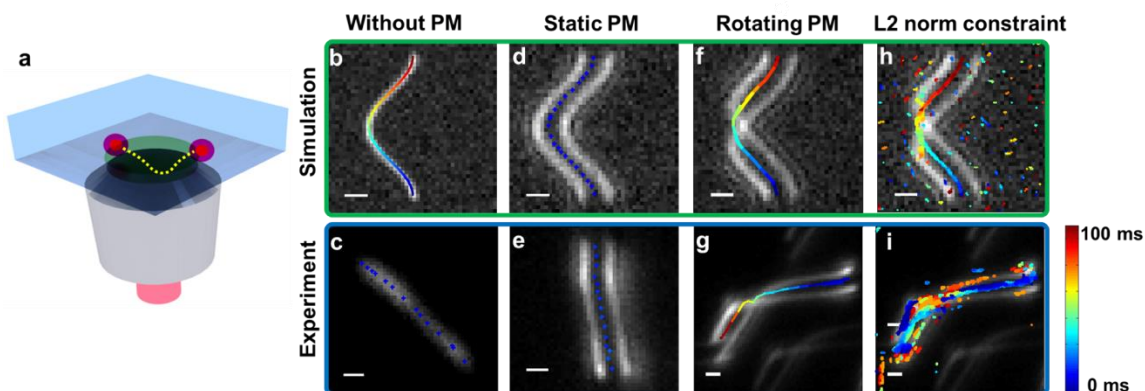


Figure 2.4: STReM resolves fast 2D transport by combining with an ADMM recovery algorithm. (a) Cartoon showing the simulation trajectory. A fluorescent emitter is simulated moving in a cosine wave constrained to the 2D plane of the surface (to simulate observation on a TIRF microscope). (b, c) Simulated and experimental frames of 2D transport without a DHPM. The ground truth time-resolved trajectory is plotted in (b) and the recovered trajectory is plotted in (c). (d, e) Simulated and experimental frames of 2D transport with a static DHPM. The crosses denote the recovered super-resolved 2D spatial positions. (f, g) Simulated and experimental frames of 2D transport with a rotating DHPM. The trajectory is plotted by connecting each recovered position adjacent in time. The real movements in (b, d, and f) are the same. In (c, e, and g) the sample motions are made by lateral translations of a fluorescent bead on a glass cover slip, with variable translation direction and speed. The camera exposure time is 100 ms. (h, i) Recovered trajectories of 2D transport with L_2 norm constraint for both simulated and experimental data. Note lack of sparseness in recovered data using L_2 norm constraints. Scale bar = 1 μm .

Finally, we show that 2D transport can be resolved with both high spatial and temporal resolution (Figure 2.4) using STReM in combination with a convex

optimization algorithm, ADMM. A motion-blurred trajectory is generated if a fluorescent emitter moves in the x-y plane within the camera exposure time (Figure 2.4a). Extracting real emitter positions is often difficult with traditional methods, especially if the PSFs overlap within each frame. Figure 2.4b, d, and f are simulated frames of a fluorescent emitter moving along a cosine wave trajectory. In Figure 2.4b, the motion-blurred image is overlain with the ground truth trajectory labeled by the colored crosses. The trajectory with a static DHPM is recovered with the ADMM algorithm, one of the advanced localization methods to analyze aggregated super-resolution data [38, 40, 78]. The ADMM algorithm is chosen because it converges at fast speed due to the closed-form expression in each iteration. Also, the ADMM algorithm requires less memory than methods such as the primal-dual interior-point method [29]. Without the ADMM algorithm the raw image to be analyzed is usually constrained in size to 10 by 10 pixels per analysis iteration [39, 40]. 2D super-localization is possible with a static DHPM, but the temporal resolution is still the camera exposure time (Figure 2.4d). When the DHPM is rotated, simultaneous super spatiotemporal resolution is achieved with ADMM algorithm (Figure 2.4f). By running 1000 Monte Carlo simulations of different 2D directed transport, the temporal resolution is demonstrated to be improved ~ 20 times better than the camera frame rate without compromising the spatial resolution of emitter localization.

STReM with ADMM is used to extract 2D localization either with a standard Gaussian PSF or with the DH PSF of the same orientation. In both cases, dynamic

information is already lacking in the collected raw images. The encoded time information is extracted in Figure 2.4g by applying ADMM to solve an L_1 norm constrained optimization problem to a rotating DHPM. With an L_2 norm constrained ADMM algorithm, numerous artifacts deviating from the ground truth appear in Figure 2.4h, i. When generating a trajectory by connecting points adjacent in time, the artifacts generate large errors, which could be avoided by applying the L_1 norm constraints.

Several potential methods will help to improve the temporal resolution of STReM. The temporal resolution for the simulations and measurements shown here is ~ 5 ms, determined by the fitting error and the intrinsic error. Further improvement is possible by rotating the DHPM faster, as long as the SNR is high enough and the camera exposure time can be tuned to match half of the rotation period. The photon budget is an important concern, especially when a single dye is used, due to its lower signal to noise ratio (SNR) compared to analytes with multiple emitters. Monte Carlo simulations comparing the effect of decreasing SNR on the temporal resolution provide insight on the useful range and limitations of STReM. The simulations show that above $\text{SNR} = 2$, the temporal resolution improvement is maintained. Further simulations evaluate the temporal resolution as a function of the dynamics of the fluorescent emitters and rotational rate of the DHPM. Thus, it would help to push the limitation of the temporal resolution of STReM by increasing the number and brightness of the probe molecules. Finally, although we demonstrate here that the combination of signal enhancement and L_1 norm

constraint optimization can fit the simulated and experimental results well, it is expected that future advanced image processing techniques will further improve the temporal resolution.

2.5. Error Analyses

2.5.1. Simulations for fast adsorption/desorption and 2D transport

Simulated experiments were conducted to estimate fitting errors of PSF orientation in fast adsorption/desorption experiments and 2D transport. In the simulation of fast adsorption/desorption, the emitter is assumed to arrive at the substrate at different times that follow a uniform distribution $P(T) = T/100 \text{ ms}, T \in [0, 100 \text{ ms})$. The surface residence time is short, ranging from 0.5 ms to 1 ms. The 2D lateral positions of the adsorption sites are randomly chosen following a uniform distribution. The appearance time of the emitter is obtained by fitting the orientation of the DH PSFs with the modified single molecule identification program[77]. In the simulation of 2D directed transport experiments, the emitter trajectory follows the 2D spatial distribution at different times as below:

$$P(X) = X/(2 \cdot X_m), X \in [-X_m, X_m), X_m = 0.28 \text{ pixels}$$

$$P(Y) = Y/(Y_m), Y \in [0, Y_m), Y_m = 0.55 \text{ pixels}$$

Each emitter is assumed to emit 200 photons per 1 ms and the background noise is simulated as a Poisson distribution of different mean value based on the

corresponding SNR (SNR ranging from 2 to 20). It should be pointed out that the orientation variation caused by the TIRF excitation mode is not considered in the simulation. Since the final uncertainty of the temporal information is composed of the fitting error and the systemic error, they should be calculated separately.

2.5.2. Application of Compressive Sensing to super-resolution localization

Compressive sensing is a signal processing technique that stores and recovers high resolution signals from low resolution signal sources. In compressive sensing, signals to be dealt with are sparse, which means most elements of the signals are zero or relatively small compared to non-zero elements. A small number of key coefficients (the non-zero elements) are able to characterize the signal. By only recording the key coefficients, the data size decreases dramatically with the compressive sensing techniques. When recovering signals with compressive sensing, the goal is to determine those key coefficients from the measured signal. The non-sparse signal can also have sparse representation after a transformation such as a Fourier or wavelet transform.

$$y = Ax$$

Equation 2.1 - domain transformation

In super-resolution microscopy the compressive sensing problem is expressed as Equation (2.1), in which y denotes the encoded raw images collected in experiment; the measurement matrix A records the raw images in which all the

possible molecule positions may exist; and x denotes the vectorised real molecule positions to be recovered in high spatial resolution. In super-resolution microscopy the recovered signal x is sparse in the spatial domain so that compressive sensing can be directly applied to improve the spatial resolution[40]. Compressive sensing reconstructs the signal by solving the L_1 norm constrained minimization problem shown in Equation (2.2).

$$\min \sum_i |c_i x_i|, \text{ s. t. } \sum_i |(A * x)_i - b_i|^2 < D \text{ and } x \geq 0$$

Equation 2.2 – L_1 norm constrained problem

In Equation (2.2) x_i and $(A * x)_i$ denote the i th element in vector x and $A * x$; $*$ denotes the convolution operation; b_i denotes i th element in measurement b ; D is a threshold related to the noise level; c_i is the weight coefficients. By applying the L_1 norm constrained minimization the recovery rate is high and over-fitting problems are avoided.

2.5.3. Alternating direction method of multipliers (ADMM) algorithm

The ADMM algorithm can be applied to solve convex optimization problems, such as L_1 norm constrained optimization. It converges at fast speeds by decomposing the original problem into several segmented optimization problems. The localization problem in super-resolution microscopy can be solved by the ADMM algorithm with a high recovery rate and low over-fitting. The raw image is

represented as the convolution between the PSF and the emitter positions in Equation (2.3):

$$y = A * x$$

Equation 2.3 – Image convolution with kernels

where y and x are the raw image in low resolution and the emitter position to be recovered in high resolution respectively. $*$ denotes the convolution operation. Spatial localization with ADMM sets A as a 2D or 3D matrix that contains a series of PSFs in 2D or 3D space. In STReM, however, A contains PSFs not only at different 2D spatial positions, but also PSFs at different times. The PSFs are generated by simulating the DH phase mask at different orientations, which corresponds to different times. Twenty one DH PSFs of varying orientations build up the measurement matrix in STReM.

To localize the emitter in high precision, x is reconstructed by the ‘deconvolution’ of y with A through the L_1 norm minimization problem in Equation (2.4).

$$\min ||c_i x_i||_1, \text{ s. t. } ||(A * x)_c - y||_2^2 < D \text{ and } x \geq 0$$

Equation 2.4 – L_2 norm constrained problem

in which $(\cdot)_c$ corresponds to the central layer among the 3D resulting frames and D is a threshold on the error. Directly solving the problem in Equation (2.4) is slow

and requires significant computational resources. The ADMM algorithm simplifies the problem by decomposing the optimization problem and the final optimization problem is expressed in Equation (2.5):

$$\min. \frac{1}{2} \|y - u_0\|_2^2 + \lambda \|u_1\|_1 + \frac{\mu}{2} \|u_0 - A * x - \eta_0\|_2^2 + \frac{\nu}{2} \|u_1 - x - \eta_1\|_2^2$$

Equation 2.5 – Augmented Lagrangian. λ , μ and ν are relaxation parameters and we use $\lambda = 0.005$, $\mu = 1$, and $\nu = 20$; η_0 , η_1 , u_0 and u_1 represent the simplified optimization problem of solving x from Equation (4.4).

2.5.4. The inapplicability of traditional video Compressive Sensing to super-resolution microscopy

Video Compressive Sensing in traditional photography is experimentally implemented in the spatial domain mostly using a spatial light modulator, such as a DMD. In a DMD, two states, “on” and “off”, are available by reflecting the incident light in two different directions, of which only signal from one of them are collected by a photon detector. The DMD is then applied to build up a random binary matrix composed of “zeros” or “ones”. The random binary matrix is demonstrated to be incoherent with most of the bases. The incoherence allows sufficient encoding during data collection and stable recovery of the original image [79]. However, half of the photons are blocked when building the binary random matrix, which leads to low photon efficiency. The number of photons collected by a photon detector is closely related to the spatial localization accuracy in microscopy [22, 45]:

$$\sigma_{2d} = \frac{c}{\sqrt{N}}$$

Equation 2.6 – Spatial resolution and photon number

in which N denotes the number of photons collected by the camera and C is a constant related to the microscope. Therefore, the installation of a DMD sacrifices spatial resolution thus inhibiting applications to super-resolution microscopy.

2.5.5. Definition of temporal resolution in STReM

The temporal resolution of STReM is defined as the uncertainty of fitting the orientation of corresponding DH PSFs, which is comprised of the fitting error and the systemic error:

$$t_b = T \times \sqrt{err_{\text{fit}}^2 + err_{\text{in}}^2}$$

Equation 2.7 – Best time resolution in STReM

$$err_{\text{fit}} = \frac{err_{\text{or}}}{180}$$

Equation 2.8 – Fitting error of time in STReM

in which t_b denotes the temporal resolution; T denotes the camera exposure time, err_{in} denotes the intrinsic error term, err_{fit} denotes the fitting error in time, and err_{or} denotes the fitting error in DH PSFs orientation by single PSF fitting or ADMM algorithm.

The fitting error in the temporal domain was obtained from Monte Carlo Simulations for both transient adsorption/desorption experiments and continuous 2D transport of fluorescent emitters (Figure 2.5). In the simulation of fast dynamics the emitters randomly adsorbed and desorbed on the surface at different times, producing a SNR of 10. The arrival time of each emitter was recovered by fitting the orientation of DH PSF. The fitting error of fast dynamics is ~ 2.0 ms (Figure 2.5 a) out of 100 ms camera exposure time. In the simulation of directed 2D transport the emitter was moved along a line with different speed. Both the spatial and temporal information are recovered with the ADMM recovery algorithm. The fitting error is ~ 2.4 ms in time and 65 nm in spatial (Figure 2.5 b, c).

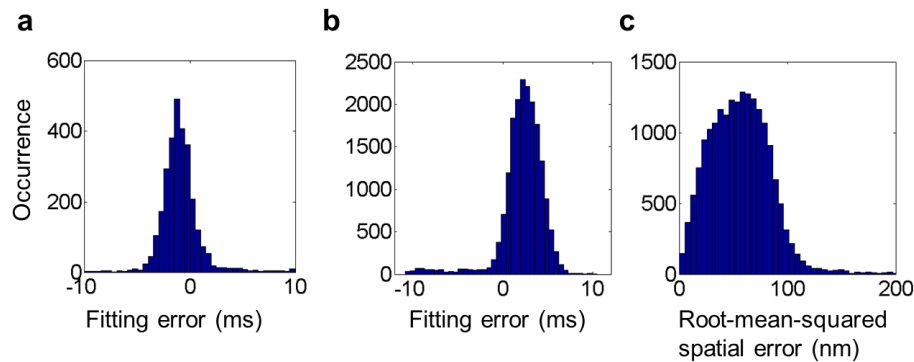


Figure 2.5 The fitting errors of fast adsorption/desorption experiments and motion-blurred trajectories with ADMM algorithm from 1000 Monte Carlo simulations. The standard deviation of the error distribution in time for single DH PSF fitting (a) and ADMM (b) are ~ 2.0 ms and ~ 2.4 ms respectively. The spatial error with ADMM is shown in (c) with the standard deviation being 65 nm.

The laser intensity distribution along the z direction in TIRF excitation mode follows an exponential decay, resulting in the fact that depth information cannot be completely excluded. Therefore the PSF orientation can also change as a result of different emitter depth, which has an effect on the time detection. The width of the depth distribution with a static DHPM serves as the control to determine systemic error present in STReM. To measure the systemic error 1000 frames, 512×512 pixel, of fluorescent beads were collected in TIRF excitation mode with a static phase mask. The PSFs are orientated slightly differently as a result of the depth variation of the emitters. The orientation of the PSFs is obtained by fitting the two lobes and then determining their centers for lateral localization. Figure 2.6a plots the CDF of the PSF orientations from 1000 experimental frames (in blue) and the fitting curve (in red) with an exponential distribution. Figure 2.6b plots the probability distribution function of the PSF orientations and fitting curve based on the fitting result of CDF. The standard deviation of the orientation distribution from the experimental results is ~ 8 degrees out of 180 degrees, corresponding to the error in time being $\sim 4.5\%$ of the camera exposure time.

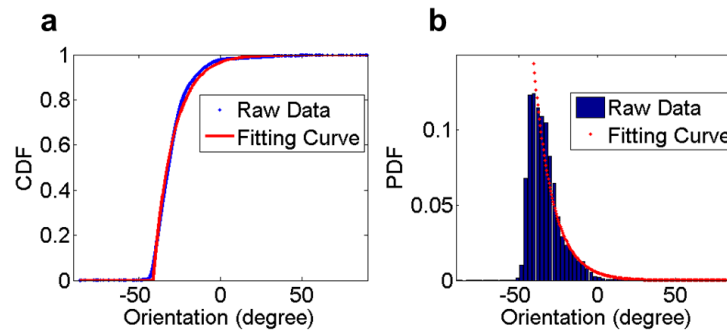


Figure 2.6 Systemic error analysis. (a) The cumulative distribution functions (CDF) of DH PSF orientation from 1000 experimental frames with static phase mask and fitting curve with exponential decay model. The $1/e$ error is ~ 8 degrees out of 180 degrees, corresponding to the intrinsic error of STReM, $\sim 5\%$ of the camera exposure time. (b) The probability density function (PDF) of the same events in (a). The red curve fits the PSF orientation distribution with an exponential decay model.

When the camera exposure time is 100 ms, the temporal resolution was then calculated to be ~ 5 ms for fast adsorption/desorption and ~ 5 ms for directed 2D transport, which leads to a temporal improvement of 20 times in comparison to the camera frame rate.

2.5.6. The temporal resolution limit of STReM

The temporal resolution can be improved by increasing the camera frame rate as long as the frame rate matches the rotation speed of the rotary mount. From Equation (2.7), the camera exposure time has a direct impact on the temporal resolution. Hence shorter exposure times lead to improved temporal resolution. Moreover, the fitting error decreases when using a shorter camera exposure time. Traditionally, increasing the camera exposure time improves the SNR of immobilized emitter linearly. However, the signal of a fast moving emitter is not enhanced even when the camera exposure time is increased, which is caused by the fact that the photon intensity on each camera pixel does not change. At the same time, the background noise increases with longer integration time. Hence a shorter

camera exposure time (T) leads to better SNR and a higher temporal resolution for the same emitter movement.

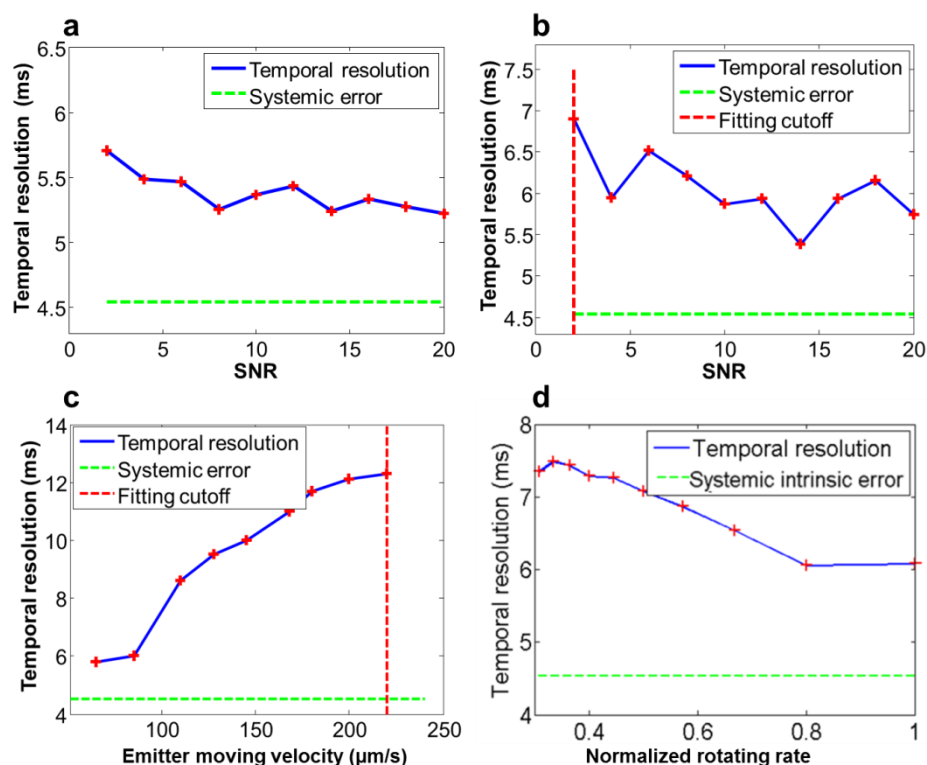


Figure 2.7 Temporal resolution of STReM for emitters with different SNR and moving velocities, and varying rotational speed of the DHPM calculated by Monte Carlo simulations. (a) The fitting error from simulated fast adsorption/desorption experiments. (b) The fitting error from simulated 2D transport experiments with ADMM recovery algorithm. The red dashed line indicates a cutoff for the fitting algorithm. (c) The temporal resolution of STReM for emitters of different translational velocities. The red line indicates a cutoff for the STReM for the simulated emitter. The cutoff can be pushed towards a higher moving speed with a brighter dye molecule. (d) The temporal resolution of STReM for different rotation speed of DHPM. The rotation speed was normalized by 300 rpm. The camera exposure time in (a) – (d) was 100 ms.

Emitters with slower movement speed can be resolved with higher temporal resolution. Each single camera pixel captures fewer photons when the fluorescent emitter moves faster, which decreases the SNR. Figure 2.7a plots the temporal resolution of STReM when capturing 2D emitter transport with different movement speeds from simulations. In the simulation each emitter is assumed to emit 3,000 photons per millisecond and Poisson noise ($var = 1500$) is added to each frame. The fitting error is combined with the systemic error to calculate the temporal resolution. The results show that faster emitters are difficult to capture and the temporal resolution decreases, which is consistent with the knowledge in traditional microscopy.

STReM can still encode time information when the phase mask rotates less than 180 degrees within one camera exposure time, but the temporal resolution will decrease. As discussed previously, the DHPM is rotated 180 degrees within each camera exposure time to keep the monotonic relationship between the orientation of the DH PSFs and the corresponding labeling time. In fact the monotonic relationship still exists when the rotation range of the DHPM is smaller than 180 degree. The temporal resolution decreases as the DHPM rotates slower, as shown in Figure 2.7b. The decrease of temporal resolution at slow rotation speed can be explained by the coherence of the measurement matrix in compressive sensing, which is a metric to test the recovery result. To easily understand the coherence, it measures the largest similarity between PSFs at different times and is calculated through:

$$M = \max_{1 \leq i \neq j \leq m} |a_i^H a_j|$$

Equation 2.9 – Coherence between two matrices

in which a_i and a_j denote columns in the matrix; ‘ H ’ means conjugate transpose operation. Larger coherence corresponds to a tougher requirement to recover the signal. The coherence between PSFs of different orientation (different time) is larger if the DHPM rotates slower. Hence the temporal resolution drops with slower DHPM rotation speed.

2.5.7. Arc-shaped PSF analysis

The length of the arc-shaped PSF is fitted to precisely extract the surface dwell time of emitter adsorption. For an arc-shaped PSF as shown in Figure 2.8, it is equivalent to fit the starting and ending orientation of the two arcs. Using a hard threshold based on the pixel intensity of the PSFs barely reaches the ground truth. In our fitting method, data is fitted by maximizing the following objective function:

$$F = \frac{|E(I_{a1}) - E(I_{a2})|}{\sqrt{\frac{1}{l_{a1}} + \frac{1}{l_{a2}}}}$$

Equation 2.10 – Single metric for arc separation

in which I_{a1} and I_{a2} denote the intensity of two regions that are divided by the fitting orientation lines; $E(\cdot)$ denotes the expected value; l_{a1} and l_{a2} denote the lengths of

two divided regions and the summation equals to half of the perimeter. Basically, large intensity difference between two divided regions implies higher probability to reach the real fitting of the arcs. However only referencing the intensity difference is not enough for us to obtain the ground truth fitting. In some situations the result deviates considerably from the ground truth when the value on several pixel values is extremely large or small, caused by the fluctuation of photon counts. To avoid this situation, we further refined the objective function by multiplying a weight factor. In the situation in which one fitting region is extremely large (l_{a1} is large) while the other one (l_{a2}) is very small, the weight factor becomes small and the corresponding fitting result is suppressed. A 2D map of the objective function value is plotted in Figure 2.8c. The starting and ending of the arcs then can be fitted by localizing the largest value on the 2D map, with the final result in Figure 2.8b. By running 1000 Monte Carlo simulations, the error of fitting the arc-shaped PSF is plotted in Figure 2.8d. When combined with the systemic error, the error to determine the surface dwell time is ~ 10 ms.

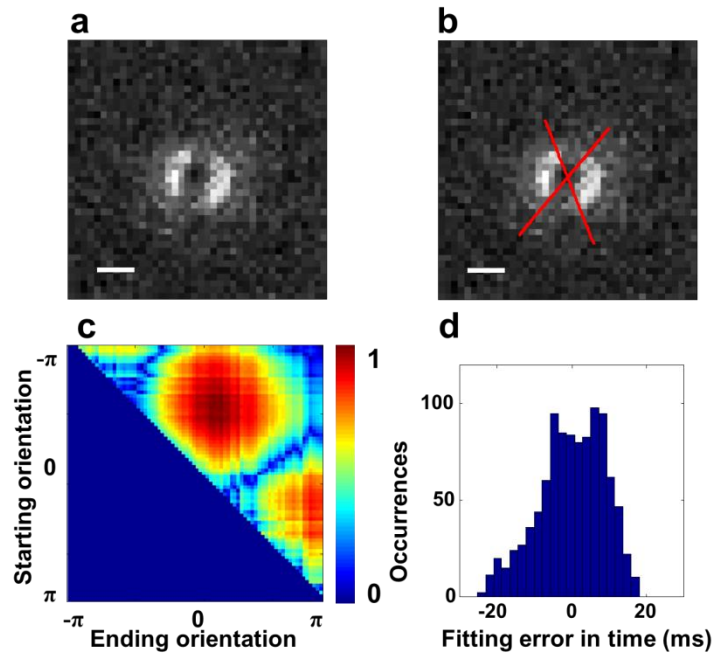


Figure 2.8 The fitting of arc-shaped PSFs and error analysis. (a) Raw experimental data of α -lactalbumin adsorbed on clean coverslip. (b) The length fitting of arc-shaped PSF. Scale bar = 1 μm . (c) The objective function value in a 2D map with different starting and ending orientations of the arc. Highest value of the objective function corresponds to orientation of separating two arcs. (d) Fitting error in time of arc-shaped PSF from 1000 Monte Carlo simulations. The standard deviation error of fitting the arc-shaped PSF is ~ 9.4 ms out of 100 ms exposure time.

2.5.8. L_2 norm constraint

The L_1 norm constrained objective function guarantees the precision of recovery result for fast 2D transport trajectory. L_1 norm optimization minimizes the L_1 norm (absolute value) of the objective function, which results in the sparsity being minimized. The L_2 norm is also widely used in data analysis and image processing, in which the mean squared value of the objective function is minimized.

In order to demonstrate the superiority of L_1 norm minimization for our method, we applied the L_2 norm in our data analysis. The recovered trajectory using a L_2 norm constraint is shown in Figure 2.9a, b. Figure 2.9a contains numerous artifacts, which cause errors when connecting the spots that are adjacent in time. More importantly, the recovered trajectory is not super-resolved spatially, with multiple recovered spots surrounding the group truth position. This is caused by the fact that the L_2 norm minimization tries to minimize the energy of the system: the system prefers the solution that contains aggregated points of low intensity rather than the single, sparse recovery result of high intensity. By connecting the aggregated points that are also close in time, it forms an incorrect wobbling trajectory, as shown in Figure 2.9c. The recovery result from L_2 norm minimization deviates from the ground truth, while L_1 norm minimization provides a solution to approach the sparse result. By comparing the recovery rate (true recovery / total recovery) and false negative rate (wrong recovery / total recovery) with both L_1 and L_2 norm constraint, it is clear that L_1 norm constraint provides a more stable and precise recovery result.

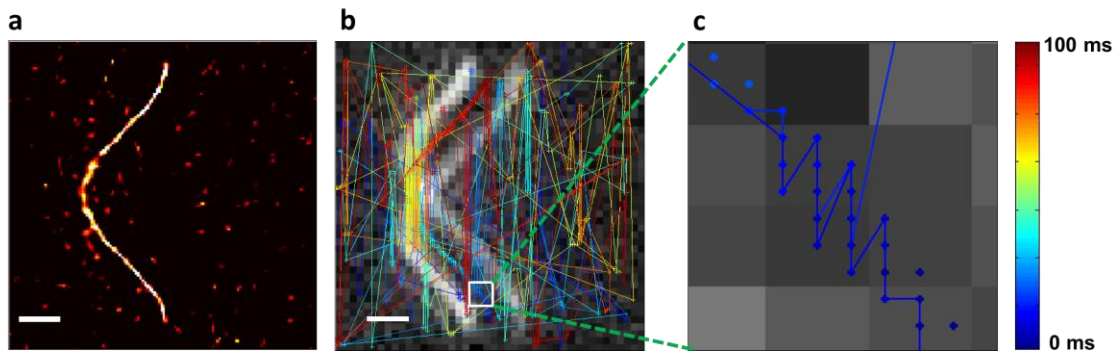


Figure 2.9 Recovered results of simulated 2D motion blurred trajectories with L_2 norm constraint. (a) The recovery results of 2D motion blurred trajectories with L_2 norm constrained optimization. The results of L_2 norm optimization contain numerous artifacts, as expected. (b) Recovered time trajectory by connecting points adjacent in time. (c) Incorrect wobbling trajectory generated from L_2 norm minimization from the highlighted region in b. Scale bar = 1 μm .

2.6. Conclusion

In this work we report STReM, in which the temporal resolution is enhanced by rotating a DHPM within a 4f system. It is worthwhile to note that the STReM method could also be implemented in any optical setup capable of encoding time information in the PSF such as those with spatial light modulators [61, 80]. The kinetic study of α -lactalbumin adsorption on a glass coverslip demonstrates that new dynamics are revealed when STReM is used to measure protein adsorption to a glass coverslip. STReM, in combination with ADMM, is demonstrated to recover accurate positions from both simulated and experimental data in the recovery of transient adsorption/desorption dynamics and fast 2D transport. The temporal resolution is improved about 20 times compared with the temporal resolution of conventional data collection.

Chapter 3

Super-temporal resolved microscopy reveals multistep desorption kinetics of α -lactalbumin from nylon

3.1. Abstract

Insight into the mechanisms driving protein-polymer interactions is constantly improving due to advances in experimental and computational methods. In this work, we used super-temporal resolved microscopy (STReM) to study the interfacial kinetics of a globular protein, α -lactalbumin (α -LA), adsorbing at the water-nylon 6,6 interface. The improved temporal resolution of STReM revealed that residence time distributions involve an additional step in the desorption process. Increasing the ionic strength in the bulk solution accelerated the desorption rate of α -LA, attributed to adsorption-induced conformational changes.

Ensemble circular dichroism (CD) measurements were used to support a consecutive reaction mechanism. Without the improved temporal resolution of STReM, the desorption intermediate was not resolvable, highlighting both STReM's potential to uncover new kinetic mechanisms and the continuing need to push for better time and space resolution.

3.2. Introduction

Controlling protein-polymer interactions is important for drug delivery, biocompatible implants, and protein separations [81-85]. Protein-polymer interactions are a challenge to study because both the protein and polymer are macromolecules that can exhibit dynamic structures [86-89]. Single molecule fluorescence spectroscopy is well suited for studying such interactions as well as other heterogeneous and dynamic processes [90-94]. Advances in super-localization methods allow for further improvements in identifying complicated kinetics hidden in macroscopic measurements [13, 95, 96], while achieving a spatial precision of tens of nanometers [4-6, 28, 75, 97-101].

Although constant progress is made in ultra-sensitive photon detectors, one area for improvement is temporal resolution because a trade-off exists between native frame rates and throughput of measurements [102, 103]. Commonly available scientific cameras can monitor hundreds of molecules simultaneously with a practical temporal resolution of ~ 10 ms [34], whereas protein-polymer dynamics can occur at time scales faster than the camera's resolution [30, 104-106].

Additionally, it can be cost-prohibitive to replace a scientific imaging camera to acquire incrementally improved time resolution. Therefore, new and affordable techniques are still needed to capture fast kinetics [107].

Recently developed super-temporal resolved microscopy (STReM) is an affordable method to enhance the temporal resolution of high throughput measurements [30]. STReM extracts sub-frame dynamics to achieve a 20-fold faster temporal resolution relative to the native frame rate of a standard scientific camera [30]. STReM sacrifices roughly 20 ~ 40 nm in spatial resolution, but still allows for spatial localization well below the diffraction limit of light [30]. STReM can be easily integrated into conventional wide-field microscopy systems without purchasing costly fast cameras. Here, STReM is utilized to study the interactions of fluorescently labeled α -lactalbumin (α -LA) at thin nylon 6,6 film surfaces. α -LA is a globular protein abundant in mammalian milk [108] and nylon 6,6 is a commonly used polymeric material in membranes [98]. These two macromolecules create a model system for the kinetic study of protein-polymer interactions. STReM's enhanced temporal resolution reveals a previously hidden intermediate state for adsorbed α -LA prior to desorption from the nylon 6,6 interface. STReM and circular dichroism results suggest that the intermediate is likely the result of near-field forces such as Van der Waals interactions between α -LA and nylon 6,6, inducing adsorptive structural rearrangement of α -LA.

3.3. Materials and methods

3.3.1. α -LA labeling

The target protein α -LA was labeled by the Willson group at University of Houston. The labeling protocol was detailed in our previous publications[13]. To increase the signal to noise ratio, each protein molecule was labeled with three Alexa 546 molecules. For single molecule measurements, 50 μ L of 63 pM α -LA in 10 mM HEPES buffer (pH = 7.3) was drop cast on the thin nylon 6,6 film.

3.3.2. Nylon 6,6 film preparation

Microscope coverslips (22 \times 22 mm, No. 1; VWR) were sequentially sonicated for 5 minutes in DI water, ethanol, and acetone. Coverslips were then soaked in a base piranha solution for 20 min at 80 $^{\circ}$ C to chemically etch the outmost atomic layer of the glass. After thoroughly rinsing the coverslips with DI water the coverslips were treated with oxygen plasma for 3 minutes (PDC-32G; Harrick Plasma, Ithaca, NY). Thin nylon 6,6 film were prepared by spin coating a 1.5 wt% nylon 6,6/formic acid solution at 3,000 rpm for 60 s (200CBX; Brewer Science Cee, Rolla, MO) on cleaned coverslips. 0.5 ml 1.5 wt% nylon 6,6/formic acid solution was gradually added into water under vigorous stirring. The precipitate was filtered and thoroughly rinsed using an 8 μ m sized filter paper. After that, the precipitate was re-dispersed in water to form nylon bead solution [109].

3.3.3. Single molecule STReM measurements

The experimental setup of STReM is shown in Figure 1 in the main text. A 532 nm laser beam (Coherent, Compass 315 M- 100SL) was focused at the back edge of an objective (Carl- Zeiss, alpha Plan-Fluar, NA = 1.45, magnification = 100×), to achieve a total internal reflection (TIR) excitation. As a result of the TIR excitation only fluorescent molecules at the polymer-solution interface were excited [13, 98]. Fluorescent signals are collected by the objective and focused by a tube lens (focal length = 165 mm). The 1st image plane is followed by a 4f system which is comprised of two 4f lenses (focal length = 75 mm) with a phase mask (Double Helix LLC, Double Helix PSF phase mask) located at 2f after the first lens. The engineered signal is re-focused on the 2nd image plane and imaged by a sCMOS camera (Hamamatsu, ORCA-Flash 4.0) operating at 100 ms per frame. A point emitter generates a Gaussian shape PSF at the 1st image plane that is converted into a double helix (DH) PSF at the 2nd image plane. As the phase mask rotates, the corresponding PSF for a point emitter rotates accordingly. Within one camera exposure the phase mask is rotated 180° so that each PSF orientation is uniquely related to the time it appeared. Super-temporal information is thus encoded in the orientations of the final PSFs.

3.3.4. Circular Dichroism Spectroscopy

Protein secondary structure data was obtained using a Jasco J-810 spectropolarimeter. Measurements of each solution were conducted at room

temperature from wavelengths of 190 to 250 nm with a scan speed of 20 nm/min in a 0.01 cm quartz cuvette. Data was obtained in millidegrees and was averaged over 10 accumulations with a data pitch of 0.1 nm. Millidegrees were converted to molar residue ellipticity ($[\theta]$) using the equation $[\theta] = \frac{\theta}{l \times N \times c \times 10}$, where θ is ellipticity in degrees, l is the path length of the cuvette in cm, N is the number of residues in the protein, and c is the concentration of the protein in g/cm³.

3.3.5. Scanning electron microscope (SEM) imaging

Nylon 6,6 microspheres were imaged with a magnification of 15,000X (FEI Quanta 400) . The dwell time was 30 μ s and the accelerating voltage was 15.0 kV. The nylon 6,6 microspheres were drop casted on a piece of glass coverslip (22 \times 22 mm, No. 1; VWR) and dried in air for 5 hours. Then a layer of gold of 5 nm was deposited on the sample surface using a sputtering system (Desk V sputtering system, Denton Vacuum).

3.3.6. Drifting α -LA events on nylon 6,6 film

Asymmetric PSFs are observed in α -LA desorption experiments, which is assumed to be caused by the drifting of α -LA within one camera exposure time. The PSFs of immobile events either produce a donut shaped PSF for long residing events or a symmetric arc shaped PSF for fast sub-frame desorption events. However, the PSF becomes complicated and asymmetric if the emitter moves in the lateral plane during one camera exposure. Out of 15,978 detected single events, 5% of them have distorted PSFs (Figure 3.1). To confirm the origin of these distorted PSFs we

simulated molecules drifting in (velocity = 1.72 nm / ms) different directions within one exposure. The corresponding PSFs of the simulated drifting molecules generated by a rotating phase mask are similar to the experimentally observed ones (Figure 3.1), which confirms that the distorted PSFs are likely due to the short-range drifting. However, without *a priori* knowledge of the in-plane diffusion, these distorted PSFs are challenging to fit and extrapolate the diffusion details. It is worth noting that these drifting molecules generate Gaussian-like PSFs with traditional microscope techniques (Figure 3.2 insets), therefore drifting cannot be easily identified with other super-resolution imaging techniques such as PALM and STORM. With STReM, the signatures of drifting molecules are intensified (Figure 3.2 A-C).

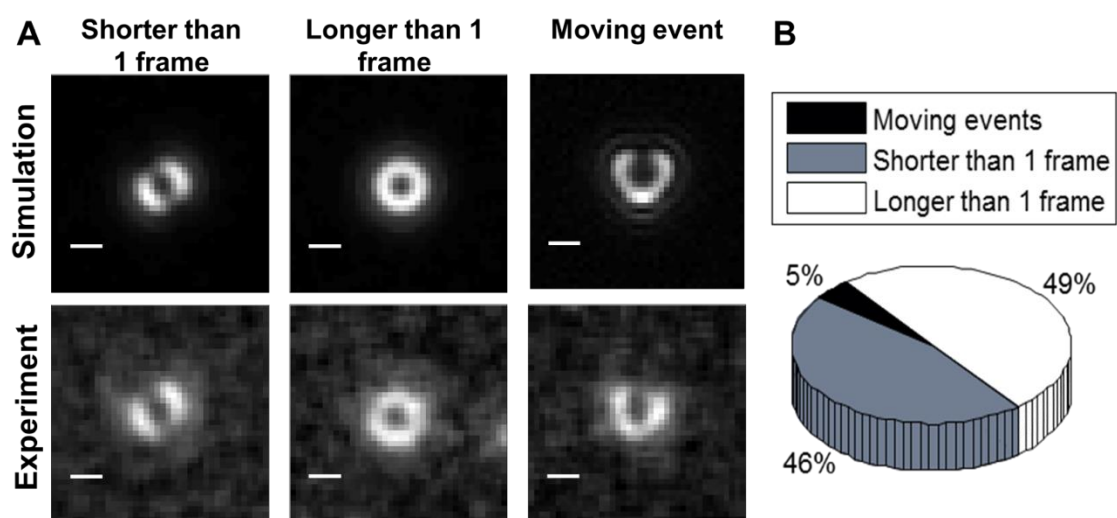


Figure 3.1. Different possible adsorption behaviors in simulations and experiments. (A) Simulated (first row) and experimental PSFs (second row) of adsorbed α -LAs that adsorb on the interface for shorter than 1 frame, longer than 1 frame, and drift. (B) Percentage of drifting events, adsorption events

that last for less than 1 camera frame, and adsorption events that last for longer than 1 camera frame.

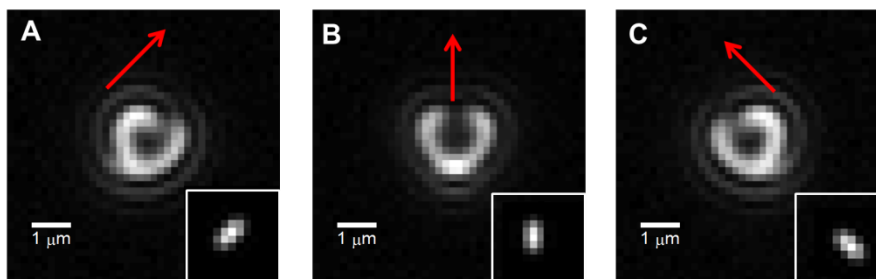


Figure 3.2. Simulated distorted STReM PSFs. (A-C) of slow in plane emitter diffusion in different directions indicated with red arrows. Insets (A-C) within each figure are the same simulated PSF taken with a traditional microscope.

To differentiate the distorted PSFs from the symmetric ones, an intensity threshold was applied to identify the number of gaps within each PSF. The arc-shaped PSFs and donut PSFs have two gaps or no gaps in the PSF respectively. However, distorted PSFs exhibit one gap making them easily identified (Figure 3.3). Distorted PSFs are thus distinguished by counting the number of gaps along the arc of the resulting PSF (Figure 3.3). Three representative experimental PSFs are showed in Figure 3.3 A, C, and E. The corresponding binary image (Figure 3.3 B, D, and F) was generated by setting a hard intensity threshold at $0.57 \times \text{maximum pixel counts}$. Distorted PSFs have only 1 gap (Figure 3.3 F), while PSFs of immobile events exhibit either 0 or 2 gaps (Figure 3.3 B, D).

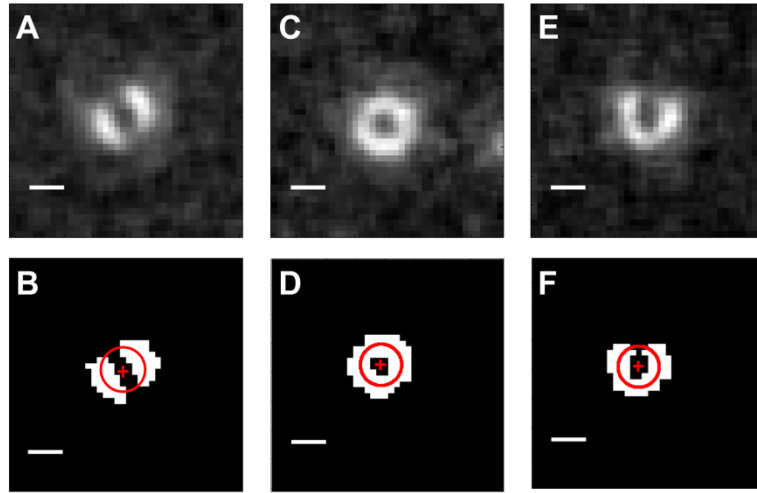


Figure 3.3. Distorted PSF identification via intensity thresholding. (A) The PSF of an immobile adsorption event lasting for less than 1 frame and the resulting (B) binary image after the intensity threshold. The red circle in B is used to count the number of gaps in the resulting PSF, with the centroid shown with the red crosshair. (C) PSF of event that lasts for more than 1 frame and the resulting (D) binary image. No gaps are found in this PSF. (E) Distorted PSF caused by drifting and (F) binary image showing only one gap in the resulting PSF. Scale bar = 1 μm .

Our intensity threshold is determined by testing 1,000 simulated PSFs with a known ground truth. Half of the simulated PSFs are immobilized containing either arc-shaped PSFs or donut-shaped PSFs, and the other half contain distorted PSFs of random emitter drifting directions with the same velocity of 1.72 nm / ms. The x axis in Figure 3.4 denotes a threshold k , and the intensity threshold applied on the pixel is calculated by " $k^{-1} \times$ the maximum pixel value". The accuracy and the misclassification rate for detecting distorted PSF are calculated as below:

$$\text{Accuracy} = \frac{\text{Num.of correctly classified distorted PSF}}{\text{Total Num.of distorted PSF}}$$

$$\text{Misclassification rate} = \frac{\text{Num.of incorrectly classified distorted PSF}}{\text{Total Num.of distorted PSF}}$$

The final intensity threshold is chosen as $0.57 \times$ maximum pixel value by picking the threshold corresponding the highest classification accuracy.

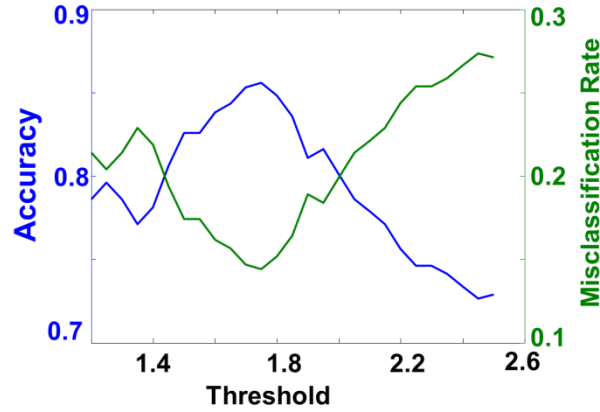


Figure 3.4 - Accuracy and misclassification rate in detecting distorted PSFs using different intensity thresholds.

3.4. Results and discussion

The addition of a stationary phase mask in the Fourier plane (Figure 3.5) changes the shape of the PSF from a Gaussian to a double helix [24, 25]. In STReM, the phase mask rotates 180° with every camera exposure, causing the PSF to rotate accordingly (Figure 3.5) [30]. The angle of the PSF reflects the arrival time (Figure 3.5B), while the arc length of the PSF reports the surface residence time (SRT) (Figure 3.5C-D), (Equation 3.1).

$$\tau_{\alpha\text{-LA}} = \frac{L_{\text{arc}}}{L_{\text{half-circle}}} \cdot T_{\text{exposure}}$$

Equation 3.1 – Surface residence time calculation

The orientation of the PSF in STReM thus encodes both adsorption and desorption kinetics with sub-camera frame temporal resolution. 95% of the almost 16,000 α -LA – nylon 6,6 interactions in the current work exhibited quantifiable adsorption/desorption dwell times.

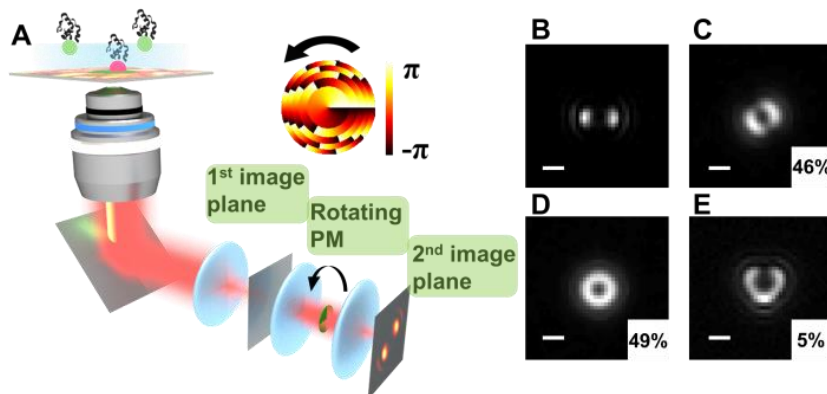


Figure 3.5. Experimental setup of STReM and simulated PSFs in STReM. (A) STReM experimental setup. Fluorescently tagged α -LA proteins at the water-polymer interface are excited with a total-internal-reflection geometry. Fluorescence is transferred into the Fourier domain after the 1st image plane and sub-frame dynamics are encoded in the resulting PSFs by a rotating phase mask [24, 25]. The final image is captured by a sCMOS at the 2nd image plane. (B - E) Simulated PSFs observed in STReM. (B) The angle of the PSF reflects the arrival time; (C) the arc length encodes the dwell time for events shorter than one frame versus (D) longer than one frame. 95% of almost 16,000 α -LA adsorption events were classified under these two types of adsorption/desorption. (E) Simulated PSF for 2D motion, exhibited by 5% of

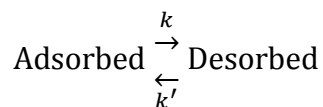
α -LA adsorption events. The insets in (C - E) denote their percent contribution in experiments and scale bar = 1 μ m.

As shown in Figure 3.5E, asymmetric PSFs result from 2D motion during adsorption. 5% of α -LA – nylon 6,6 interactions were classified as involving 2D motion, which is reported to occur and even dominate in some interfacial systems [69, 110]. Traditional super-resolution imaging techniques such as PALM and STORM fit each PSF with a 2D Gaussian to extract its centroid [4-6]. Molecules exhibiting sub-frame 2D motion can be fit with 2D Gaussian functions, but the direction of motion is not attainable. With STReM, the PSFs of molecules exhibiting 2D motion are asymmetric, which makes them readily distinguishable from stationary molecules and encodes information about the direction and path of motion. Analyzing such distorted PSFs is challenging, but is achievable as we have demonstrated previously [30]. Because the α -LA – nylon 6,6 interactions reported here were dominated by simple adsorption/desorption, events with 2D motion were excluded for the mechanistic analysis that follows.

α -LA adsorption statistics at nylon 6,6 surfaces were collected with and without STReM, and depending on the protein and salt concentrations, as many as 46% of the 15,978 adsorption events exhibited a SRT faster than the camera exposure time. The temporal resolution was limited to 100 ms without STReM, which was the native exposure time for the sCMOS camera. With the same exposure time, STReM provided a temporal resolution of ~ 5 ms [30].

Figure 3.6 shows a wide-field image with three different PSFs. Each PSF was analyzed for initial angle and arc lengths (Figure 3.6B – D), providing dwell time statistics. The donut shaped PSF in Figure 3.6D reflects a protein with a dwell time longer than a single frame, in which case SRT was determined by accumulating its PSF arc lengths in all consecutive frames.

STReM SRT statistics for α -LA at nylon 6,6 were compared with those extracted with the native camera frame rate (Figure 3.6E-F). Using the frame exposure time of the camera, the SRT distribution was easily fit with single exponential decay (Figure 3.6E), consistent with a pseudo-first order/first order adsorption/desorption mechanism for the α -LA interaction with a nylon 6,6 surface Equation (3.2) [111, 112]. The probability density function for such process is shown in Equation (3.3).



Equation 3.2 – Simple adsorption/desorption model

$$P(t) = k \exp(-kt)$$

Equation 3.3 – Residence time distribution

Fitting the experimental results with Equation 3.3 yielded a desorption rate constant of $6.7 \pm 0.5 \text{ s}^{-1}$.

STReM, with its faster time resolution, instead revealed SRT statistics with an initial rise followed by a decay (Figure 3.6F). This SRT distribution suggests that there are at least two steps in the desorption process [96, 113-115]. The presence of a second kinetic process could be caused by the α -LA molecules adapting an intermediate state before desorption [116]. Such kinetics are observed in enzyme-catalyzed Michaelis-Menten reactions [113, 114], nanoparticle catalysis [96], DNA unwinding [115], and virus fusion [117]. In those cases, an intermediate state was proposed to account for the two-term exponential distribution exhibiting an initial rise followed by a decay shown in the SRT distributions. It is expected that heterogeneities exist among surface binding sites.

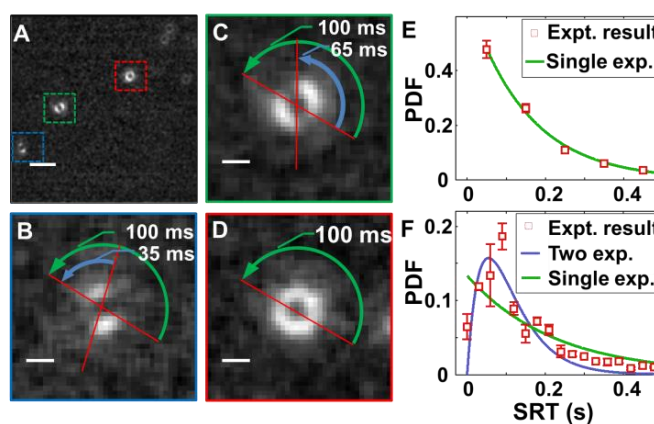
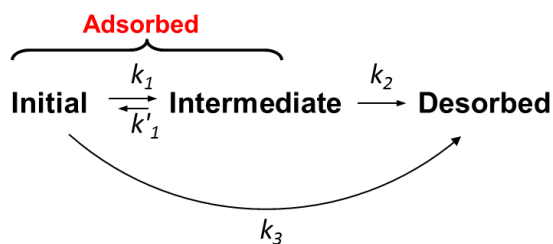


Figure 3.6. Kinetic analysis of α -LA adsorption on nylon 6,6 film with STReM. (A) Representative STReM single frame containing sub-frame (blue and green) and longer (red) protein adsorption events. (B - D) Zoomed PSFs in (A). The surface residence time (SRT) is determined from the arc length of the PSF shown with the blue arrows in (B), and (C). The green arrows denote one camera exposure of 100 ms. For events longer than one frame such as (D), the SRT is determined by cumulating its PSF arc lengths in all consecutive frames. (E, F) The probability distribution function (PDF) of SRT for adsorbing α -LA on

thin nylon 6,6 film without (E) and with STReM (F). The data in (E) is fit with a single exponential decay function, while the data in (F) can only be fit with a two-term exponential function. Scale bar is 5 μm in (A) and 1 μm in (B-D).

We propose a consecutive reaction model to explain observed SRT distributions acquired from STReM Scheme (3.1).



Scheme 3.1. Consecutive reaction model for α -LA desorption

In this scheme, Initial refers to α -LA upon adsorption, and we propose an Intermediate state that precedes a Desorbed protein. Initial and Intermediate are emissive states detectable by STReM, while Desorbed is a motion blurred state that cannot be detected. There are thus two possible pathways for a single α -LA to desorb, direct desorption with a single rate constant (k_3), or a two-step desorption following rate constants k_1 and k_2 respectively. Based on the SRT distributions shown in Figure 3.6F, we may assume k_3 is much smaller than $k_1 + k_2$. Thus, we can set $k_3 = 0$ to remove the direct desorption pathway. Furthermore, it is also possible to neglect the reverse process in the first step (k_{-1}) by comparing our experimental SRT distributions to alternate theoretical models [116, 118, 119]. Consequently, the

overall mechanism becomes a two-step desorption model with one intermediate state. This intermediate state might be due to conformational changes of α -LA [75], or reorientation at the surface binding site [120]. Steady-state conditions do not apply here to derive the SRT distribution because the intermediate state concentration cannot be treated as constant. The probability density function for this model is calculated in Equation (3.4):[119]

$$P(t) = \frac{k_1 k_2}{k_1 - k_2} \times [\exp(-k_2 t) - \exp(-k_1 t)]$$

Equation 3.4 – Residence time distribution of proposed model

The two rate constants k_1 and k_2 are extracted by fitting the experimental result with Equation 3.4. The initial rise in SRT distributions is associated with k_1 , which is the faster step in desorption. k_2 , on the other hand, is associated with the tail of the SRT distributions. By fitting the SRT distribution with Equation 3.4 the rate constant k_1 and k_2 are calculated to be $31 \pm 5 \text{ s}^{-1}$ and $8 \pm 2 \text{ s}^{-1}$. It is worth noting that the rate constant k ($6.7 \pm 0.5 \text{ s}^{-1}$) extracted from the single exponential decay without STReM in Figure 2E is close to k_2 extracted with STReM ($8 \pm 2 \text{ s}^{-1}$). This is because the limited temporal resolution (100 ms) can only resolve the slow component of the process.

Electrostatics, which can dominate protein-polymer interactions [121, 122], were found not to drive the consecutive desorption kinetics for α -LA and nylon 6,6 (Figure 3.7). SRTs were acquired at a range of sodium chloride concentrations

and fit with Equation 3.4 (Figure 3.7A). Both k_1 and k_2 increased with increasing ionic strength (Figure 3.7B), leading to an overall faster desorption process. It is well known that high salt concentrations can effectively shield electrostatic interactions between adsorbate and adsorbent [95, 123, 124]. In our case, both α -LA and nylon 6,6 carry net negative charge at pH 7.3 [123, 125, 126]. Increasing the ionic strength in the bulk solution should shield electrostatic repulsion and yield longer SRTs, in direct contrast to our results. Therefore we conclude that electrostatic interactions do not play a significant role in the desorption process.

Instead, circular dichroism analyses [127, 128] suggest that the desorption mechanism of α -LA from nylon 6,6 is dictated by near-field forces rather than long range electrostatic forces (Figure 3.7C), consistent with one recent study [123]. To replicate STReM experimental conditions, micron sized nylon 6,6 beads were synthesized and suspended in aqueous solution with α -LA. Whereas the nylon bead sample did not produce a CD signal, free α -LA produced a CD spectrum consistent with the native alpha helical secondary structure [129, 130]. In the presence of nylon beads, the residual ellipticity from α -LA exhibited greater amplitude, indicating that adsorption induced increased alpha helical secondary structure α -LA [129, 130]. A protein with alpha helical secondary structure will exhibit two negative peaks at roughly 222 nm and 208 nm and a positive peak at 192 nm [131]. α -LA is composed of dominantly alpha helical secondary structural motifs, but also includes beta sheets and random coils thereby slightly shifting these spectral features. The slight differences in MRE seen from 190 to 195 nm is due to the

presence of NaCl which absorbs light in this spectral region [132]. The increased signal in the negative peaks, as well as a shift to shorter wavelengths in those negative peaks suggests that α -LA is adopting a more folded alpha helical state in the presence of salt and nylon. Finally, whereas no significant conformational changes were observed when α -LA was exposed to higher salt concentrations, in the presence of nylon beads, salt further enhanced the alpha helical structure.

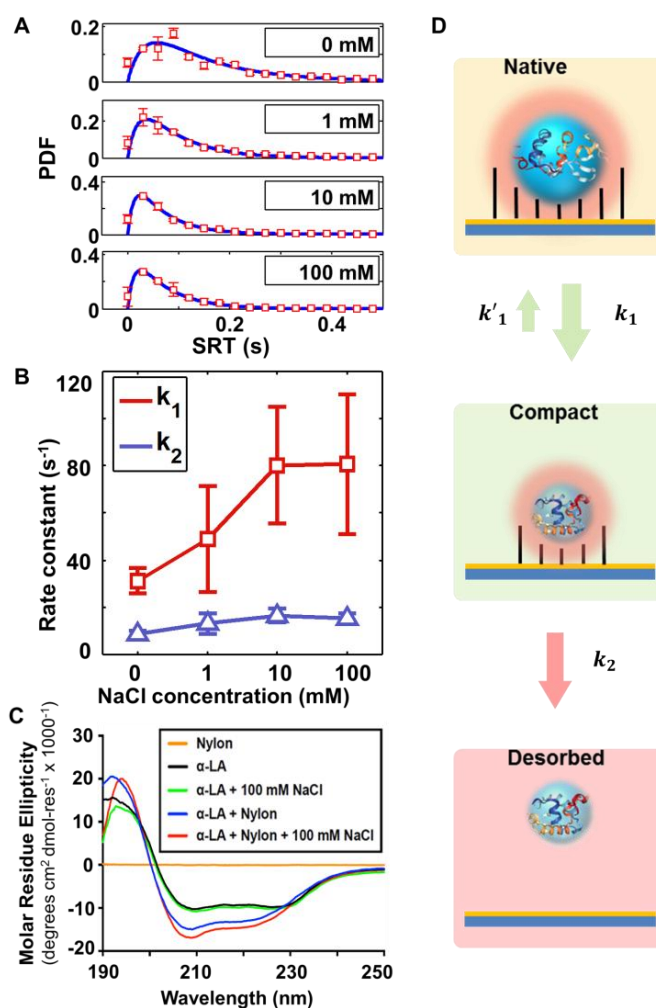


Figure 3.7. α -LA desorption and structural changes in the presence of sodium chloride. (A) SRT distributions for single α -LA molecules under various

sodium chloride concentrations. Blue curves are fit using Eq. 4. (B) The fitted rate constants are plotted versus different sodium chloride concentrations. (C) Circular dichroism measurements of α -LA in various experimental conditions. Error bars in (A) and (B) are standard deviations from three different trials containing 8,000 frames respectively. (D) Cartoon depicting the proposed desorption mechanism. The black lines indicate the interaction between proteins and the nylon surface.

The combined single molecule kinetic analyses and CD measurements lead us to propose a near-field force-driven consecutive reaction mechanism for α -LA desorption from nylon interfaces (Figure 3.7D). After α -LA adsorbs to nylon 6,6, it undergoes a fast conformational change, only observable with the faster time resolution of STReM, to form a more defined alpha helical structure. The conformational change yields a decreased surface area for the interaction α -LA and nylon, since the protein is more tightly folded [133]. The decrease in near-field interaction is a necessary intermediate before α -LA desorption, an effect that is exacerbated at high ionic strengths.

3.5. Conclusion

In this work, STReM was used to study the interfacial kinetics of α -LA at nylon 6,6 films. We observed that a majority of proteins were immobilized at binding sites, while only a small portion of proteins exhibited 2D motion. With the enhanced temporal resolution of STReM, we identified an intermediate state in the desorption process. Kinetic analyses coupled with CD spectroscopy suggested that the intermediate was a more tightly folded form of α -LA upon interaction with the

nylon surface. Increasing the ionic strength in the bulk solution further increased the alpha helical structure of α -LA, thereby increasing both desorption rate constants. We envision that the enhanced temporal resolution of STReM will bring increased insights into the mechanisms driving protein-surface interactions, with a range of applications.

Chapter 4

A generalized method to design phase masks for 4D super-resolution microscopy

4.1. Abstract

Point spread function engineering by phase modulation is a novel approach to 3D super-resolution microscopy, with different point spread functions proposed for specific applications. It is often not easy to achieve the desired shape of engineered point spread functions because of the challenge to determine the correct phase mask. Additionally, a phase mask can either encode 3D space information or additional time information, but not both simultaneously. A robust algorithm for recovering a phase mask to generate arbitrary point spread functions is needed. In this work, a generalized phase mask design method is introduced by performing an

optimization. A stochastic gradient descent algorithm and a Gauss-Newton algorithm are developed and compared for their ability to recover the phase mask designs for previously reported point spread functions. The new Gauss-Newton algorithm converges to a minimum at much higher speeds. This algorithm is used to design a novel stretching-lobe phase mask to encode temporal and 3D spatial information simultaneously. The stretching-lobe phase mask and other masks are fabricated in-house for proof-of-concept using multi-level light lithography and an optimized commercially sourced stretching-lobe PM is validated experimentally to encode 3D spatial and temporal information. The generalizability of the algorithms is further demonstrated by generating a phase mask that comprises 4 different letters at different depths.

4.2. Introduction

Recent years have witnessed the development of wavefront phase manipulation for various optical applications including manipulating plasmonic nanoantennas [134, 135], holographic displays [136, 137], and engineered PSFs for depth detection [24-26, 138, 139]. Phase-only modulation is advantageous in single-molecule studies because it minimizes lost photons [51], thereby maintaining a high spatial resolution [140]. Super-resolution techniques accomplished by point spread function (PSF) engineering simultaneously provide large axial detection ranges and high 3D spatial resolutions [29, 49, 51, 97, 141-143]. To achieve 3D super-resolution detection with such methods, a 4f optical geometry is used, and a phase mask (PM)

is inserted into the Fourier plane between two lenses along the detection path of a traditional optical microscope. The emission signal is modified in the Fourier domain by the PM within the 4f system [61]. Several previously reported PMs generate PSFs containing depth-dependent information and are used for the imaging of biological structures and dynamics in 3D space [49, 53, 97, 141, 144-148]. More recently, the popular double helix PM was used to encode temporal dynamics, but at the cost of sacrificing 3D spatial information [30, 149].

Designing new or complicated PMs is a phase retrieval problem [25, 150-152] in that recovering a signal's representation in the Fourier domain from only the amplitude in spatial domain is computationally challenging. Previous approaches for phase retrieval include Gerchberg-Saxton algorithms [150, 153] and hybrid input-output algorithms [154]. In most cases, a PM is designed by optimizing only a single image in the spatial domain. However, to achieve 3D detection, the continuous evolution of the PSF throughout the desired depth range needs to be considered in the PM design. This requirement limits the application of existing algorithms in the design of novel PMs.

PM design utilizing Gaussian-Laguerre modes is one of the methods that yields a PM design with continuously evolving PSFs [25]. However, this algorithm is only applicable for rotating PSFs, while non-rotating functional PSFs cannot be generated with this method. Additionally, PM design method using Gaussian-Laguerre modes requires *a priori* information, which is not always obtainable. The

above challenges motivate the necessity for a generalized and robust method for the design of PMs suitable for a wide array of imaging applications.

Here we report two new algorithms for PM design using the fundamentals of optimization: a stochastic gradient descent algorithm and a Gauss-Newton algorithm [155]. To confirm the validity of these methods, two well-known PSFs and corresponding PMs are recovered with our method. The patterns generated by our algorithms match well to the previously reported PSFs [25]. We further propose a novel stretching-lobe PSF for super-resolution localization using our algorithms. This PSF is capable of simultaneously encoding sub-frame temporal information while achieving 3D super-localization. Moreover, we showcase the ability to encode arbitrarily complex PSFs by designing a single PM that yields PSFs with the individual letters “R”, “I”, “C”, “E” at different depths. The physical PMs are fabricated via photolithography for proof-of-concept, and the chosen stretching-lobe PM is sourced commercially for final implementation.

4.3. Methods

4.3.1. Phase retrieval

One of the most critical applications of PMs lies in super-resolution microscopy, thus we emphasize encoding super-localization information in PSFs, and formatting the PM design problem as a phase retrieval problem. As shown in Figure 4.1, PSF engineering is accomplished with a 4f system in a microscopes

detection path. The PM is located at the Fourier plane, which is centered between two lenses. After phase modulation by the PM, the emission light is transferred back to the spatial domain and captured by a camera. The intensity profile of PSFs generated by a given PM is expressed as the following:

$$I_{(i,j)} = \left| \left\{ FFT \left[mask_{cir} \circ \exp(1i \cdot P) \right] \right\}_{(i,j)} \right|^2$$

Equation 4.1 – Relationship between phase mask and PSF

in which $I(\cdot)$ is the intensity distribution and the subscript (i, j) denotes the pixel located at i^{th} row and j^{th} column; $FFT(\cdot)$ is the discrete fast Fourier transform operation; $mask_{cir}$ is a pupil intensity mask; P is the PM pattern in the Fourier domain. Our aim is to calculate the PM P from the intensity distribution of the desired PSFs, $I(x)$, which is equivalent to an inverse process of that in Equation (4.1). However, a simple inverse Fourier transform of the PSF cannot reconstruct the PM because the phase information of the PSF is lost and only its amplitude is recovered.

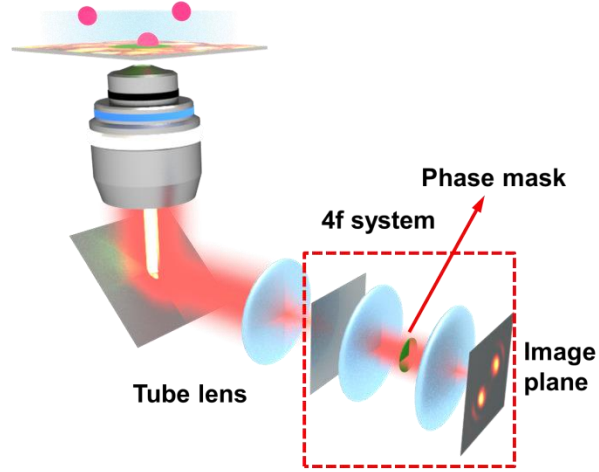


Figure 4.1. Layout of a typical PM based 3D super-resolution microscope. The 4f system is shown in the red box consisting of two lenses and a PM at the Fourier plane. Emission light is modulated by the 4f system and projected to a camera.

Here we propose a scheme to inversely retrieve the PM pattern by minimizing the difference between the input PSF profile and the PSF derived from the PM (Equation (4.1)). The PM is successfully generated when the two PSFs match with each other as shown in Equation (4.2):

$$I(x)|_p = \bar{d}$$

Equation 4.2 – Phase mask design equation

in which $I(x)|_p$ is the PSF calculated from the PM and \bar{d} is the desired PSF containing different depths. To do so, an optimization method is applied. The residual, difference between two PSF intensity profiles, is calculated by:

$$\begin{aligned}
 \overrightarrow{r(f)} &= \left\| |I(x)|^2 - d \right\|_2^2 \\
 &= \left\| \left\{ FFT \left[mask_{cir} \circ \exp(1i \cdot P(f)) \right] \right\}^2 - d \right\|_2^2
 \end{aligned}$$

Equation 4.3 – Residual function

where $||$ is an operation of taking the element-wise amplitude squared; ' \circ ' is the Hadamard product operator. Then the corresponding PM is calculated by minimizing the objective function $F(f)$:

$$F(f) = \frac{1}{2} \left\| \overrightarrow{r(f)} \right\|_2^2$$

Equation 4.4 – Objective loss function

4.3.2. Converting phase retrieval to a standard optimization problem

PM retrieval is simplified by converting the original problem to a standard linear optimization problem. It should be noted that Equation (4.5) cannot be directly solved because of the existence of a Fourier transform. In most optimization problems a gradient of the objective function needs to be calculated, which is computationally challenging when a Fourier transform is applied to the objective function. We first represent the discrete Fourier transform with matrix multiplication. Then two algorithms are proven in this manuscript to recover PM

designs for desired PSFs. One utilizes a Stochastic Gradient Descent (SGD) algorithm and the second algorithm relies on a Gauss-Newton method using 2nd order approximation.

$$P = \underset{P}{\operatorname{argmin}} F(f) = \underset{P}{\operatorname{argmin}} \frac{1}{2} \left\| \overrightarrow{r(f)} \right\|_2^2$$

Equation 4.5 – Phase mask calculation

The 2D discrete Fourier transform is equivalent to the product of matrix multiplication by the Fourier transform matrix \overrightarrow{H} and the PM pattern $\overrightarrow{P(f)}$:

$$\overrightarrow{X} = \overrightarrow{H} \cdot \overrightarrow{P(f)}$$

Equation 4.6 – Fourier transform represented by matrix multiplication

$$\overrightarrow{H} = \begin{bmatrix} \exp\left(-2\pi i \times (1-1) \times \frac{1-1}{N}\right) & \cdots & \exp\left(-2\pi i \times (1-1) \times \frac{N-1}{N}\right) \\ \vdots & \ddots & \vdots \\ \exp\left(-2\pi i \times (K-1) \times \frac{1-1}{N}\right) & \cdots & \exp\left(-2\pi i \times (K-1) \times \frac{N-1}{N}\right) \end{bmatrix}$$

Equation 4.7 – Fourier transform operation matrix

in which \overrightarrow{x} denotes the amplitude of signal in the spatial domain and $\overrightarrow{P(f)}$ denotes the vectorised PM pattern. The dimension of the Fourier matrix \overrightarrow{H} is determined by

the image size of the PSF (K) and the image size of the PM (N) in Equation (4.7).

Thus the residual is expressed by:

$$\begin{aligned} r(f) &= \left\| |I(x)|^2 - d \right\|_2^2 \\ &= \left\| H \cdot \left(mask_{cir} \circ \exp(1i \cdot P(f)) \right) \right\|_2^2 - d \right\|_2^2 \end{aligned}$$

Equation 4.8 – Re-formatting the phase mask design problem

4.3.3. SGD optimization

SGD algorithm is widely used in solving optimization problems, especially when there are multiple constraints applied on the objective functions simultaneously [156, 157]. In the PM design, the PSFs at different layers constrain one layer of the PM, which makes the SGD algorithm ideal for solving this problem. In each iteration the PM is updated only based on the PSF at one depth and consecutively constrain the PM at nine different layers. The gradient is calculated using Newton's difference quotient. The algorithm scheme is shown in Algorithm 4.1 below.

Algorithm 4.1 SGD

- 1: **Initialize** $P(f), iter, norm g, \alpha$
- 2: **while** ($iter < maxit$) **do**

3: Depth layer $i = \lfloor 9 \cdot rand() \rfloor$

4: $g_i(f) = \frac{F_i(f+h) - F_i(f)}{h}$

5: $P(f)^{iter+1} = P(f)^{iter} - \alpha \cdot g_i(f)$

6: $iter = iter + 1$

7: end while

8: **return** $P(f)$

4.3.4. Gauss-Newton optimization

A Gauss-Newton algorithm is applied to solve the optimization problem in Equation 4.5. Gauss-Newton methods are well known for solving linear optimization problems with fast convergence speeds. It outperforms Newton's method in terms of lower computational loads by only updating the Jacobin matrix rather than the second order derivative of the objective function:

$$J = \nabla r(f) = \begin{bmatrix} \frac{\partial r_1}{\partial f_1} & \dots & \frac{\partial r_1}{\partial f_N} \\ \vdots & \ddots & \vdots \\ \frac{\partial r_K}{\partial f_1} & \dots & \frac{\partial r_K}{\partial f_N} \end{bmatrix}$$

Equation 4.9 – Jacobian matrix

$$\nabla F(x) = J^T \cdot r(x)$$

Equation 4.10 – Gradient of objective function

in which ∇ is the gradient operator and J is the Jacobin matrix. The optimization steps are summarized in Algorithm 4.2:

Algorithm 4.2 Gauss-Newton

```

1:   Initialize  $P(f), iter, normg$ 

2:   while ( $normg > tol$  & &  $iter < maxit$ ) do

3:       Update  $F(f), r(f), J(f)$ 

4:        $P(f)^{iter+1} = P(f)^{iter} - (J^T \cdot J)^{-1} (J^T \cdot r(f))$ 

5:        $iter = iter + 1$ 

6:        $normg = \|\nabla F(f)\|_2^2 / (1 + abs(F))$ 

7:   end while

8:   return  $P(f)$ 

```

The Gauss-Newton algorithm converges much faster than SGD algorithm because of the utilization of 2nd order approximation. As the input PSF becomes more complicated, the second method is preferred to reach the minimum within a

reasonable period of time. Thus we only focus on the Gauss-Newton algorithm in the manuscript for the fabrication and experimental verification of the PM designs.

4.3.5. Fabrication of PM using reaction-ion etching (RIE)

The PMs are fabricated on fused silica substrates through nine iterations of photolithography, with Reactive Ion Etching (RIE) following each step. To perform the photolithography, photomasks are patterned on a 4 inch Soda Lime substrate via direct laser writing. A total of 9 hard mask patterns are prepared to fabricate a PM consisting of 10 layers with various thicknesses. The final PMs have pixelated patterns with pixel sizes of either $33\ \mu\text{m}$ or $50\ \mu\text{m}$ for different PSF patterns. The fabrication process is illustrated in Figure 4.2.

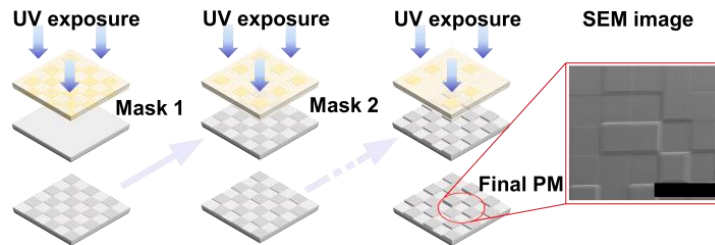


Figure 4.2. Fabrication process of the PM using photolithography. A total of nine iterations are involved with each using a different photomask. Patterns are etched to the substrates after photoresists are developed in each iteration of photolithography. Scale bar = $100\ \mu\text{m}$ in SEM image.

4.3.6. Commercial sourcing of optimized PM

A higher resolution (80 by 80 pixels) PM was purchased from Double Helix Optics (Boulder, CO) [158]. The commercially sourced PM was fabricated using gray

scale lithography techniques, allowing the etching depth on the PM to be controlled by the exposure time of a laser beam on each pixel, which yields higher depth and lateral resolutions than those used in our proof-of-concept PMs [159].

4.3.7. Depth measurement and calibration

PSFs of designed PMs are measured by imaging carboxylate-modified polystyrene 100 nm beads (orange fluorescent, max abs/em: 540/560 nm, Invitrogen) at different depths. The fluorescent samples are excited by a 532 nm laser (Coherent, Compass 315M-100SL). The signal is collected by an oil-immersion objective (Carl-Zeiss, alpha Plan-Fluar) and then imaged by a sCMOS camera (Hamamatsu, ORCA-Flash 4.0). An objective with an objective scanner (P-721 PIFOC) is applied to calibrate the depth of sample. A high resolution (80 x 80 pixel) PM stretching-lobe PM, purchased from Double Helix LLC, is mounted on a motorized rotary mount (QIOPTIQ, Rotary Mount with Servo Motor) and the rotating speed is 300 rpm.

4.4. Results and discussion

4.4.1. Recovering well-established PMs

To test the validity of our algorithms we first generate a PM based on a commonly used engineered PSF, namely the double helix (DH) PSF. DH PSFs are rotating PSFs, and as discussed earlier, are originally designed in the Gaussian-Laguerre domain [25]. In the Gaussian-Laguerre domain the different modes are

orthogonal and form a complete basis set, and the PMs are decomposed into coefficients of the modes. The mode coefficients are optimized to derive the final PM pattern. Or proposed algorithms take a different approach as each pixel in the PM pattern is individually optimized and the final PM is obtained by simultaneously optimizing all pixels. The minimum is reached by iteratively forcing the generated PSFs to be the desired pattern.

Our algorithms are able to generate a PM pattern that can produce DH PSFs similar those previously reported [25]. The initial guess of the PM and the input PSFs are shown in Figure 4.3A-B. Unlike previous algorithms, our algorithms do not require *a priori* information. Even random initial guesses as shown in Figure 4.3A lead to convergence. The input PSFs have two Gaussian-shaped lobes that rotate around the center point (white crosses in Figure 4.3B). The PM pattern is pixelated containing 40 by 40 pixels. Thus, a total of 1,600 variables are optimized simultaneously in this algorithm. The maximum number of iterations using Gauss-Newton algorithm is set to 20, which converges to the minimum and gives reasonably good results. Figure 4.3C-D are the recovered PMs and the corresponding PSFs at different depths using our algorithms. It is worth noting that the produced PSFs have side lobes, which is similar to the previously reported DH PSFs [25]. This PM is also recovered using a Gerchberg-Saxton algorithm and SGD algorithm, but the Gerchberg-Saxton algorithm does not yield well defined DH PSFs. The PM is experimentally fabricated using the RIE method (Figure 4.3E). The fabricated PM is measured (Figure 4.3E) and the PSFs shown in Figure 4.3F are the

results of 1.0 μm fluorescent beads imaged at different axial depths. The shapes of the obtained PSFs deviate slightly from the simulated PSFs especially for the -1.125 μm depth as shown in Figure 4.3F. We attribute this deviation to missing information during the discretization of the PM in addition to artifacts generated during PM fabrication. Additionally a PM that produces previously published corkscrew PSFs [144] is also successfully recovered using our algorithms.

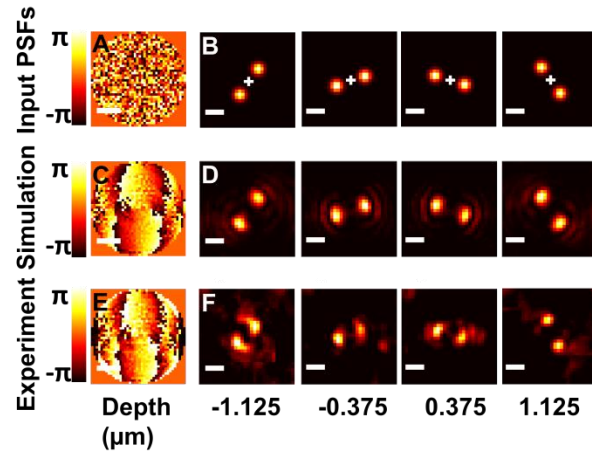


Figure 4.3. PM fabricated using RIE and corresponding DH PSFs. (A) Initial guess for the PM pattern. (B) Intensity profiles of the desired PSFs. These intensity profiles are used as the input for the PM design. Each PSF contains two Gaussian distributed lobes and the orientation varies at different depth. The white crosses denote the center position of the lobes, which is the lateral position of the emitter in 3D super-resolution microscopy. (C, D) The recovered PM (C) and its corresponding PSFs at different depths (D). (E, F) The fabricated PM (E) and the measured PSFs at different depths (F). The scale bar in A, C, and E is 500 μm and 1 μm in B, D, and F.

4.4.2. Stretching-lobe PSF to obtain both time and depth information in high resolution

Similar to rotating PSFs, the non-rotating PSFs are important for super-localizations as well. Therefore it is highly desired to use our algorithm to develop novel non-rotating PMs. Our proposed algorithm outperforms the Gaussian-Laguerre algorithm because it is not restricted to rotating PSFs. Non-rotating PSFs were reported previously. However none of them are back calculated based on the input PSFs. In specific applications the rotation response is already used for detection of information other than depth. For example in our former work [30] the PM is physically rotated within one camera exposure time so that the corresponding rotated PSF encodes sub-frame time information. In this situation, if the PM also has a rotation response to depth change, the depth information will be coupled with time information. As a result simultaneously detection of both 3D spatial and time information will not be achievable with current rotating PSFs and is addressed in our discussion of the stretching-lobe PSF proposed in this work.

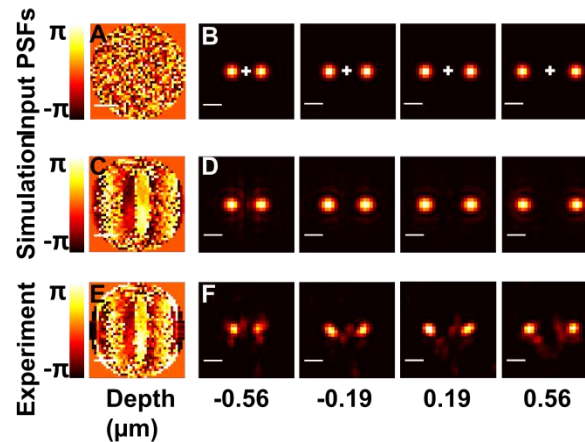


Figure 4.4. PM fabricated using RIE and corresponding stretching-lobe PSFs. (A) Initial guess for the PM pattern. (B) Intensity profiles of the desired PSF. Each PSF contains two Gaussian distributed lobes and the distance between two lobes varies at different depth. The white crosses denote the center position of the lobes, which is usually the lateral position of the emitter in 3D super-resolution microscopy. (C, D) The recovered PM (C) and its corresponding PSFs at different depths (D). (E, F) The fabricated PM (E) and the measured PSFs at different depths (F). The scale bar in A, C, and E is 500 μm and 1 μm in B, D, and F.

We propose a new stretching-lobe PSF to encode the depth response in 3D super-resolution microscopy into the distances between the two lobes of the PSFs. The desired PSFs are shown in Figure 4.4A. They consist of two Gaussian distributed lobes with the center between two lobes (white crosses) indicating the lateral position of the emitter. Once again, the PM contains 40 by 40 pixels. Instead of changing the relative orientation between the two lobes, the distance between them changes when the depth of emitter is changed (Figure 4.4B). With a random PM initial guess, the generated PM pattern (Figure 4.4C) and the corresponding PSFs produced from the PM (Figure 4.4C) are calculated. Compared to DH PSFs, the stretching-lobe PSFs have narrower depth ranges from $-0.75 \mu\text{m}$ to $0.75 \mu\text{m}$. When the emitter moves beyond the detection range, the intensity will decay rapidly until the PSF is not observable anymore. To verify this PSF experimentally the PM is also fabricated (Figure 4.5) to measure the resulting PSFs (Figure 4.4E-F). The obtained PSFs match with the simulated data reasonably well. When physically rotating the PM, the orientation will not couple with the depth dependent response and thus this

PSF is an ideal candidate for encoding both 3D spatial and high temporal information.

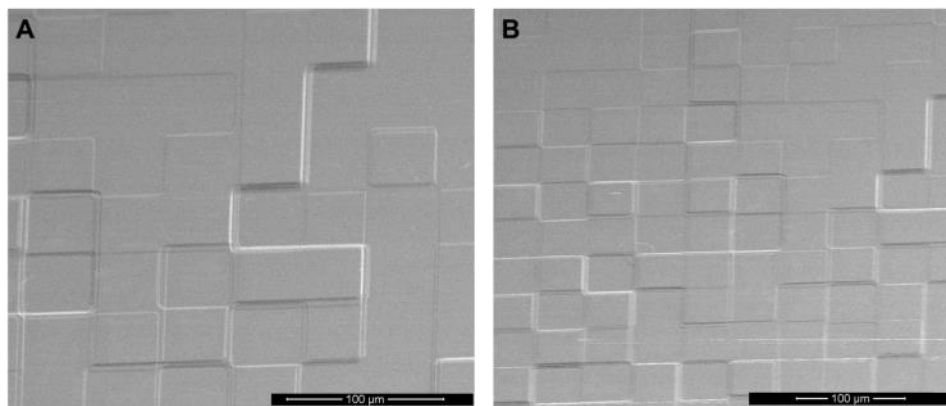


Figure 4.5. Scanning electron microscope (SEM) image of two regions on stretching-lobe PM. Different depths of the surface feature is achieved by multiple layer light-lithography.

By running Monte Carlo simulations, the localization precision of the stretching-lobe PSFs is calculated to refine the best working distances (Figure 4.6). Each fluorescent emitter is simulated to emit photons following a Poisson distribution with a mean value of 2,000 photons. Various signal to noise ratios (SNRs) are considered in this simulation as well. The stretching-lobe PSFs provide reliable 3D position localization within the depth range from $-0.6\ \mu\text{m}$ to $0.6\ \mu\text{m}$.

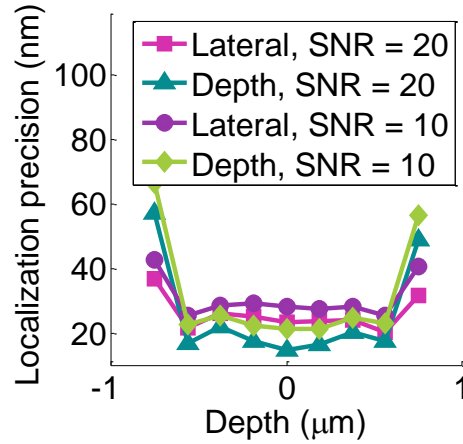


Figure 4.6. Localization precision of stretching-lobe PSFs. Localization precision in both lateral and depth directions predicted by 1,000 Monte Carlo simulations per data point.

Rotation of the stretching-lobe PM enables the simultaneous acquisition of both 3D spatial and sub-frame temporal information. As discussed in our previous works [30, 160], the depth and time response are the same for the DH PSF, leading to a rotational response when either depth or time changes. With the stretching-lobe PM, the depth response is independent of the time response, as shown in Figure 4.7. The high resolution stretching-lobe PM provides high lateral and depth resolution. The high resolution PM increases the peak intensity of PSFs by 3% compared with that in Figure 4.4C. The PSFs were imaged with a high camera frame rate (100 fps) to show that different orientations of the two lobes uniquely label time. Whereas, the emitter's depth is encoded in the distance between the two lobes, (Figure 4.7). It must be noted that in the application of sub-frame temporal retrieval, as we have previously demonstrated [30, 160], a longer frame rate would

be used resulting in PSFs with arc-lengths encoding the surface residence time. The PSFs shown in Figure 4.7 represent a single emitter at different depths and times. The development of this PSF design allows for 3D tracking to be performed in addition to resolving sub-frame temporal information all compressed into a 2D image. Using this PSF design from tracking applications will also demand the development of more advanced algorithms [29, 161] designed for such PSF shapes.

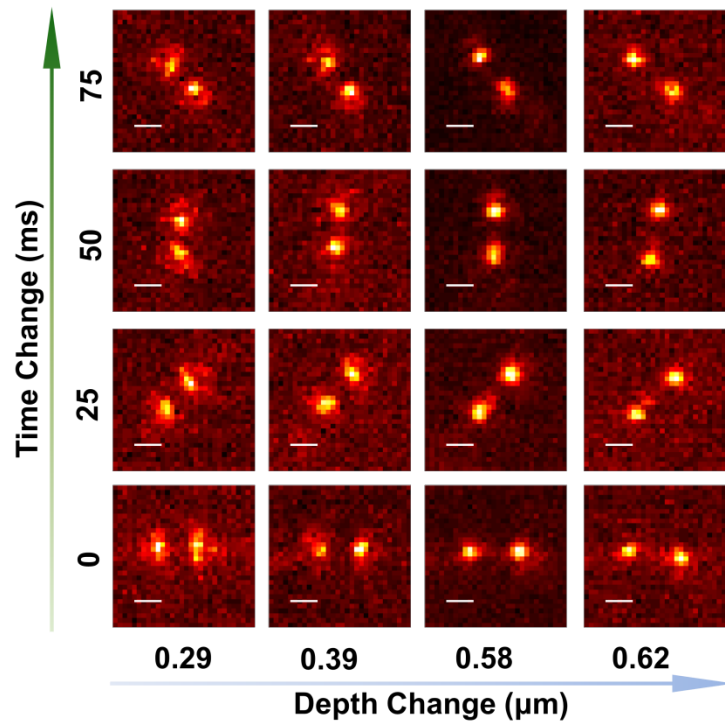


Figure 4.7. Experimental PSFs of stationary green beads when rotating the stretching-lobe PM fabricated using gray-scale lithography. PSFs of different orientations (rows) denote different time; PSFs of different lobe distance (columns) denote different depth of the emitter. The scale bar is 1 μm .

4.4.3. Developing complicated PSFs

In addition to generating 3D PSFs for depth detection, the proposed algorithm can also design complicated PSF patterns such as the spelling of arbitrary words. Figure 4.8A shows an initial PM pattern containing a 60 by 60 matrix of random initial guesses. Figure 4.8B are the input PSFs containing four letters at different depths. The number of pixels increases compared with the PMs used for the DH PSF or stretching-lobe PSF due to the fact that the desired PSFs are much more complicated and requires more granularities. Thus a finer spatial control of the PM is necessary in this application. Four different constraints are simultaneously applied to the PM design. It is usually unsolvable using traditional phase retrieval approaches. However our algorithm generates a PM based on the complicated PSF inputs of spelling the word “RICE”.

Our algorithm is robust and generalized enough to generate various different types of complicated PSFs solely based on the input PSF profiles. In Figure 4.8B, four letters are used as the desired PSFs, and the PM pattern can still be recovered (Figure 4.8C). It is clear that the four letters are successfully recovered by the PM (Figure 4.8D), although a few artifacts are involved in the end. The PM is fabricated (Figure 4.8E) and the PSFs are obtained (Figure 4.8F).

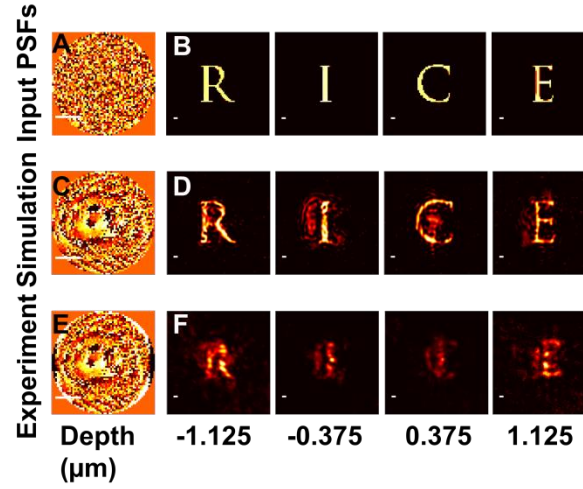


Figure 4.8 PM fabricated using RIE for complicated PSFs. (A) Initial guess for the PM pattern. (B) Intensity profiles of the desired PSF. Four letters at different depths serve as four constraints. (C, D) The recovered PM (C) and its corresponding PSFs at different depths (D). (E, F) The fabricated PM (E) and the measured PSFs at different depths (F). The scale bar is 500 μm in A, C, and E, while it equals to 1 μm in B, D, and F.

4.5. Conclusion

In this work we propose two new algorithms to design the PM for arbitrary shape of PSFs. We verify the universality of our algorithm by recovering two published PMs that were designed with a different algorithm. Later, we propose a novel stretching-lobe PSF for 3D super-resolution microscopy and generated the corresponding PM using the faster performing Gauss-Newton method. Finally, we also successfully design a PM that corresponds to very complicated PSFs at different depths.

Chapter 5

Conclusions

5.1. Summary

This thesis is focused on the application of phase modulation in super-resolution microscopy. Phase modulation modifies the phase of the signal and encodes additional information of the fluorescent emitters. Previous application of phase modulation to super-resolution microscopy, such as depth detection, was limited to the spatial domain. In this thesis, the first aim has been to extend it to the time domain by proposing STReM. By rotating the phase mask in high rotational speed, the time information can be monotonically labeled by the PSF's orientation. Combined with the compressive sensing techniques, the high spatial and temporal information embedded in 2D images can be retrieved. On one hand, STReM can be applied to the situation in which the dynamics of events are faster than the camera frame rate, and the details cannot be uncovered without STReM. On the other hand,

for the events occurring in a relatively slower time scheme, STReM can still be applied to the data collection but using a much lower camera frame rate. In the second scenario the data to be collected is decreased in size, which will be a solution to the large data size in single molecule study.

Besides extending the phase modulation to time domain, this thesis has also proposed multiple new PSF patterns to encode the depth information by using a new phase mask design algorithm. Existing phase masks can only encode a limited group of PSF patterns, such as rotating PSFs. In this thesis, a generalized and robust phase mask design method is proposed, which only requires the desired PSF patterns at different depths. New phase mask patterns are proposed, such as stretching-lobe PSFs. Complicated PSFs containing different letters at different depths are also designed to demonstrate the ability of the algorithm.

5.2. Future development

An important extension of this work is to combine the phase modulation in both depth and time encoding. An obvious drawback of the current STReM technique is that it is limited to encode fast dynamics in the 2D plane. When it comes to a complicated, fast trajectory in 3D space, the data encoding algorithm of STReM will totally fail. The problem is caused by the fact that both depth and time share the same PSF response, rotating property. In Chapter 4.4.2, a brand new PSF response is proposed to solve this problem, named stretching-lobe PSF. One emitter has two lobes for this PSF and the distance between two lobes gives depth information of the

emitter. By rotating such a phase mask, the depth information is encoded by the orientation of the PSFs while the depth information is encoded by the distance between two lobes. Thus it is theoretically achievable to obtain both 3D spatial and time information from a single 2D image. Such a 4D SReM setup will be a powerful tool to study complicated system in super-resolution study in the future!

References

1. B. Amos, "Lessons from the history of light microscopy," *Nature Cell Biology* **2**, E151 (2000).
2. N. Lane, "The unseen world: reflections on Leeuwenhoek (1677) 'Concerning little animals'," *Philosophical Transactions of the Royal Society B: Biological Sciences* **370** (2015).
3. E. H. Mercer, "A SCHEME FOR SECTION STAINING IN ELECTRON MICROSCOPY," *Journal of the Royal Microscopical Society* **81**, 179-186 (1963).
4. E. Betzig, G. H. Patterson, R. Sougrat, O. W. Lindwasser, S. Olenych, J. S. Bonifacino, M. W. Davidson, J. Lippincott-Schwartz, and H. F. Hess, "Imaging Intracellular Fluorescent Proteins at Nanometer Resolution," *Science* **313**, 1642-1645 (2006).
5. S. T. Hess, T. P. K. Girirajan, and M. D. Mason, "Ultra-High Resolution Imaging by Fluorescence Photoactivation Localization Microscopy," *Biophys. J.* **91**, 4258-4272 (2006).
6. M. J. Rust, M. Bates, and X. Zhuang, "Sub-diffraction-limit imaging by stochastic optical reconstruction microscopy (STORM)," *Nat Meth* **3**, 793-796 (2006).
7. R. Erni, M. D. Rossell, C. Kisielowski, and U. Dahmen, "Atomic-Resolution Imaging with a Sub-50-pm Electron Probe," *Physical Review Letters* **102**, 096101 (2009).
8. H. G. Rudenberg, and P. G. Rudenberg, "Chapter 6 - Origin and Background of the Invention of the Electron Microscope: Commentary and Expanded Notes on Memoir of Reinhold Rüdenberg**Reinhold Rüdenberg's memoir begins on p. 171 of this volume," in *Advances in Imaging and Electron Physics*(Elsevier, 2010), pp. 207-286.
9. N. Bohr, "The Quantum Postulate and the Recent Development of Atomic Theory1," *Nature* **121**, 580 (1928).
10. J. Rivnay, H. Wang, L. Fenno, K. Deisseroth, and G. G. Malliaras, "Next-generation probes, particles, and proteins for neural interfacing," *Science Advances* **3** (2017).
11. P. Weinberger, "Revisiting Louis de Broglie's famous 1924 paper in the *Philosophical Magazine*," *Philosophical Magazine Letters* **86**, 405-410 (2006).
12. K. Mitsuishi, M. Shimojo, M. Han, and K. Furuya, "Electron-beam-induced deposition using a subnanometer-sized probe of high-energy electrons," *Applied Physics Letters* **83**, 2064-2066 (2003).
13. L. Kisley, J. Chen, A. P. Mansur, B. Shuang, K. Kourentzi, M.-V. Poongavanam, W.-H. Chen, S. Dhamane, R. C. Willson, and C. F. Landes, "Unified superresolution experiments and stochastic theory provide mechanistic insight into protein ion-exchange adsorptive separations," *Proc. Natl. Acad. Sci. U.S.A.* **111**, 2075-2080 (2014).

14. H. Blom, and J. Widengren, "STED microscopy—towards broadened use and scope of applications," *Current Opinion in Chemical Biology* **20**, 127-133 (2014).
15. S. W. Hell, and J. Wichmann, "Breaking the diffraction resolution limit by stimulated emission: stimulated-emission-depletion fluorescence microscopy," *Opt. Lett.* **19**, 780-782 (1994).
16. E. Abbe, "Beiträge zur Theorie des Mikroskops und der mikroskopischen Wahrnehmung," *Arch. Mikrosk. Anat* **9**, 56 (1873).
17. H. Blom, and J. Widengren, "Stimulated Emission Depletion Microscopy," *Chem. Rev.* **117**, 7377-7427 (2017).
18. S. Scheffler, M. Sauer, and H. Neuweiler, "Monitoring antibody binding events in homogeneous solution by single-molecule fluorescence spectroscopy," *Zeitschrift für Physikalische Chemie* **219**, 665-678 (2005).
19. B. N. Giepmans, S. R. Adams, M. H. Ellisman, and R. Y. Tsien, "The fluorescent toolbox for assessing protein location and function," *science* **312**, 217-224 (2006).
20. G.-J. Kremers, S. G. Gilbert, P. J. Cranfill, M. W. Davidson, and D. W. Piston, "Fluorescent proteins at a glance," *J Cell Sci* **124**, 157-160 (2011).
21. P. Prabhat, Z. Gan, J. Chao, S. Ram, C. Vaccaro, S. Gibbons, R. J. Ober, and E. S. Ward, "Elucidation of intracellular recycling pathways leading to exocytosis of the Fc receptor, FcRn, by using multifocal plane microscopy," *Proc. Natl. Acad. Sci. U.S.A.* **104**, 5889-5894 (2007).
22. R. J. Ober, S. Ram, and E. S. Ward, "Localization Accuracy in Single-Molecule Microscopy," *Biophys. J.* **86**, 1185-1200 (2004).
23. B. Huang, W. Wang, M. Bates, and X. Zhuang, "Three-Dimensional Super-Resolution Imaging by Stochastic Optical Reconstruction Microscopy," *Science* **319**, 810-813 (2008).
24. S. R. P. Pavani, M. A. Thompson, J. S. Biteen, S. J. Lord, N. Liu, R. J. Twieg, R. Piestun, and W. E. Moerner, "Three-dimensional, single-molecule fluorescence imaging beyond the diffraction limit by using a double-helix point spread function," *Proc. Natl. Acad. Sci. U.S.A.* **106**, 2995-2999 (2009).
25. S. R. P. Pavani, and R. Piestun, "High-efficiency rotating point spread functions," *Opt. Express* **16**, 3484-3489 (2008).
26. A. S. Backer, and W. E. Moerner, "Extending Single-Molecule Microscopy Using Optical Fourier Processing," *J. Phys. Chem. B* **118**, 8313-8329 (2014).
27. L. Shao, P. Kner, E. H. Rego, and M. G. L. Gustafsson, "Super-resolution 3D microscopy of live whole cells using structured illumination," *Nat. Methods* **8**, 1044-1046 (2011).
28. D. Faulón Marruecos, M. Kastantin, D. K. Schwartz, and J. L. Kaar, "Dense Poly(ethylene glycol) Brushes Reduce Adsorption and Stabilize the Unfolded Conformation of Fibronectin," *Biomacromolecules* **17**, 1017-1025 (2016).
29. B. Shuang, W. Wang, H. Shen, L. J. Tauzin, C. Flatebo, J. Chen, N. A. Moringo, L. D. C. Bishop, K. F. Kelly, and C. F. Landes, "Generalized recovery algorithm for 3D super-resolution microscopy using rotating point spread functions," *Sci. Rep.* **6**, 30826 (2016).

30. W. Wang, H. Shen, B. Shuang, B. S. Hoener, L. J. Tauzin, N. A. Moringo, K. F. Kelly, and C. F. Landes, "Super Temporal-Resolved Microscopy (STReM)," *J. Phys. Chem. Lett.* **7**, 4524-4529 (2016).
31. F. Cella Zanacchi, Z. Lavagnino, M. Perrone Donnorso, A. Del Bue, L. Furia, M. Faretta, and A. Diaspro, "Live-cell 3D super-resolution imaging in thick biological samples," *Nat. Methods* **8**, 1047-1049 (2011).
32. J. S. Biteen, M. A. Thompson, N. K. Tselentis, G. R. Bowman, L. Shapiro, and W. E. Moerner, "Super-resolution imaging in live *Caulobacter crescentus* cells using photoswitchable EYFP," *Nat. Methods* **5**, 947-949 (2008).
33. M. Fernandez-Suarez, and A. Y. Ting, "Fluorescent probes for super-resolution imaging in living cells," *Nat. Rev. Mol. Cell Biol.* **9**, 929-943 (2008).
34. F. Huang, T. M. P. Hartwich, F. E. Rivera-Molina, Y. Lin, W. C. Duim, J. J. Long, P. D. Uchil, J. R. Myers, M. A. Baird, W. Mothes, M. W. Davidson, D. Toomre, and J. Bewersdorf, "Video-rate nanoscopy using sCMOS camera-specific single-molecule localization algorithms," *Nat Meth* **10**, 653-658 (2013).
35. L. Gao, J. Liang, C. Li, and L. V. Wang, "Single-shot compressed ultrafast photography at one hundred billion frames per second," *Nature* **516**, 74-77 (2014).
36. E. J. Candes, J. Romberg, and T. Tao, "Robust uncertainty principles: exact signal reconstruction from highly incomplete frequency information," *IEEE Trans. Inf. Theory* **52**, 489-509 (2006).
37. D. L. Donoho, "Compressed sensing," *IEEE Trans. Inf. Theory* **52**, 1289-1306 (2006).
38. J. Min, C. Vonesch, H. Kirshner, L. Carlini, N. Olivier, S. Holden, S. Manley, J. C. Ye, and M. Unser, "FALCON: fast and unbiased reconstruction of high-density super-resolution microscopy data," *Sci. Rep.* **4**, 4577 (2014).
39. A. Barsic, G. Grover, and R. Piestun, "Three-dimensional super-resolution and localization of dense clusters of single molecules," *Sci. Rep.* **4**, 5388 (2014).
40. L. Zhu, W. Zhang, D. Elnatan, and B. Huang, "Faster STORM using compressed sensing," *Nat. Methods* **9**, 721-723 (2012).
41. H. P. Babcock, J. R. Moffitt, Y. Cao, and X. Zhuang, "Fast compressed sensing analysis for super-resolution imaging using L1-homotopy," *Opt. Express* **21**, 28583-28596 (2013).
42. A. C. Sankaranarayanan, C. Studer, and R. G. Baraniuk, "CS-MUVI: Video compressive sensing for spatial-multiplexing cameras," in *2012 IEEE International Conference on Computational Photography (ICCP)*(2012), pp. 1-10.
43. M. F. Duarte, M. A. Davenport, D. Takhar, J. N. Laska, S. Ting, K. F. Kelly, and R. G. Baraniuk, "Single-Pixel Imaging via Compressive Sampling," *IEEE Trans. Image Process.* **25**, 83-91 (2008).
44. L. X. Tom Goldstein, Kevin F. Kelly, Richard G. Baraniuk, "The STONE Transform: Multi-Resolution Image Enhancement and Real-Time Compressive Video," *CoRR* **1311.3405** (2013).
45. S. Ram, E. S. Ward, and R. J. Ober, "How accurately can a single molecule be localized in three dimensions using a fluorescence microscope?," *Proceedings of SPIE* **5699**, 426-435 (2005).

46. A. Small, and S. Stahlheber, "Fluorophore localization algorithms for super-resolution microscopy," *Nat Meth* **11**, 267-279 (2014).
47. S. R. P. Pavani, M. A. Thompson, J. S. Biteen, S. J. Lord, N. Liu, R. J. Twieg, R. Piestun, and W. E. Moerner, "Three-dimensional, single-molecule fluorescence imaging beyond the diffraction limit by using a double-helix point spread function," *Proc. Natl. Acad. Sci. U. S. A.* **106**, 2995-2999 (2009).
48. M. D. Lew, S. F. Lee, J. L. Ptacin, M. K. Lee, R. J. Twieg, L. Shapiro, and W. E. Moerner, "Three-dimensional superresolution colocalization of intracellular protein superstructures and the cell surface in live *Caulobacter crescentus*," *Proc. Natl. Acad. Sci. U. S. A.* **108**, E1102-E1110 (2011).
49. M. D. Lew, M. A. Thompson, M. Badieirostami, and W. E. Moerner, "In vivo Three-Dimensional Superresolution Fluorescence Tracking using a Double-Helix Point Spread Function," *Proceedings of SPIE--the International Society for Optical Engineering* **7571**, 75710Z-75710Z (2010).
50. A. Greengard, Y. Y. Schechner, and R. Piestun, "Depth from diffracted rotation," *Opt. Lett.* **31**, 181-183 (2006).
51. G. Grover, S. Quirin, C. Fiedler, and R. Piestun, "Photon efficient double-helix PSF microscopy with application to 3D photo-activation localization imaging," *Biomed Opt Express* **2**, 3010-3020 (2011).
52. A. Barsic, G. Grover, and R. Piestun, "Three-dimensional super-resolution and localization of dense clusters of single molecules," *Sci Rep* **4**, 5388 (2014).
53. S. Jia, J. C. Vaughan, and X. W. Zhuang, "Isotropic Three-dimensional Super-resolution Imaging with a Self-bending Point Spread Function," *Nat Photonics* **8**, 302-306 (2014).
54. M. Okada, T. Kubo, K. Masumoto, and S. Iwanaga, "Super resolution imaging of HER2 gene amplification," (2016), pp. 97140E-97140E-97145.
55. H. Li, D. Chen, G. Xu, B. Yu, and H. Niu, "Three Dimensional Multi-molecule Tracking in Thick Samples with Extended Depth-of-field," *Opt. Express* **23**, 787-794 (2015).
56. B. Yu, J. Yu, W. Li, B. Cao, H. Li, D. Chen, and H. Niu, "Nanoscale Three-dimensional Single Particle Tracking by Light-sheet-based Double-helix Point Spread Function Microscopy," *Appl. Opt.* **55**, 449-453 (2016).
57. M. S. C. Almeida, and M. A. T. Figueiredo, "Deconvolving Images With Unknown Boundaries Using the Alternating Direction Method of Multipliers," *IEEE Trans. Image Process.* **22**, 3074-3086 (2013).
58. D. Gabay, and B. Mercier, "A dual algorithm for the solution of nonlinear variational problems via finite element approximation," *Computers & Mathematics with Applications* **2**, 17-40 (1976).
59. G. Grover, S. Quirin, C. Fiedler, and R. Piestun, "Photon efficient double-helix PSF microscopy with application to 3D photo-activation localization imaging," *Biomed. Opt. Express* **2**, 3010-3020 (2011).
60. K. Lydia, C. Wei-Shun, C. David, P. M. Andrea, and F. L. Christy, "Extending single molecule fluorescence observation time by amplitude-modulated excitation," *Methods and Applications in Fluorescence* **1**, 037001 (2013).

61. A. S. Backer, and W. E. Moerner, "Extending Single-Molecule Microscopy Using Optical Fourier Processing," *J. Phys. Chem. B* **118**, 8313-8329 (2014).
62. J. H. a. S. Monserud, Daniel K., "Interfacial Molecular Searching Using Forager Dynamics," *Phys. Rev. Lett.* **116**, 6 (2016).
63. B. Wang, S. M. Anthony, S. C. Bae, and S. Granick, "Anomalous yet Brownian," *Proceedings of the National Academy of Sciences* **106**, 15160-15164 (2009).
64. C. R. Daniels, L. Kisley, H. Kim, W.-H. Chen, M.-V. Poongavanam, C. Reznik, K. Kourentzi, R. C. Willson, and C. F. Landes, "Fluorescence correlation spectroscopy study of protein transport and dynamic interactions with clustered-charge peptide adsorbents," *Journal of Molecular Recognition* **25**, 435-442 (2012).
65. B. Shuang, D. Cooper, J. N. Taylor, L. Kisley, J. Chen, W. Wang, C. B. Li, T. Komatsuzaki, and C. F. Landes, "Fast Step Transition and State Identification (STaSI) for Discrete Single-Molecule Data Analysis," *J. Phys. Chem. Lett.* **5**, 3157-3161 (2014).
66. E. A. Permyakov, *Alpha -lactalbumin* (Nova Science Publishers, 2005).
67. H. Shen, X. Zhou, N. Zou, and P. Chen, "Single-Molecule Kinetics Reveals a Hidden Surface Reaction Intermediate in Single-Nanoparticle Catalysis," *J. Phys. Chem. C* **118**, 26902-26911 (2014).
68. N. Nelson, and D. K. Schwartz, "Specific Ion (Hofmeister) Effects on Adsorption, Desorption, and Diffusion at the Solid–Aqueous Interface," *J. Phys. Chem. Lett.* **4**, 4064-4068 (2013).
69. D. Wang, H.-Y. Chin, C. He, M. P. Stoykovich, and D. K. Schwartz, "Polymer Surface Transport Is a Combination of in-Plane Diffusion and Desorption-Mediated Flights," *ACS Macro Lett.* **5**, 509-514 (2016).
70. D. Wang, R. Hu, J. N. Mabry, B. Miao, D. T. Wu, K. Koynov, and D. K. Schwartz, "Scaling of Polymer Dynamics at an Oil–Water Interface in Regimes Dominated by Viscous Drag and Desorption-Mediated Flights," *J. Am. Chem. Soc.* **137**, 12312-12320 (2015).
71. M. J. Wirth, and D. J. Swinton, "Single-Molecule Probing of Mixed-Mode Adsorption at a Chromatographic Interface," *Anal. Chem.* **70**, 5264-5271 (1998).
72. M. J. Wirth, D. J. Swinton, and M. D. Ludes, "Adsorption and Diffusion of Single Molecules at Chromatographic Interfaces," *J. Phys. Chem. B* **107**, 6258-6268 (2003).
73. J. N. Mabry, M. J. Skaug, and D. K. Schwartz, "Single-Molecule Insights into Retention at a Reversed-Phase Chromatographic Interface," *Anal. Chem.* **86**, 9451-9458 (2014).
74. L. Kisley, and C. F. Landes, "Molecular Approaches to Chromatography Using Single Molecule Spectroscopy," *Anal. Chem.* **87**, 83-98 (2015).
75. J. S. Wertz, D. K. Schwartz, and J. L. Kaar, "Surface-Mediated Protein Unfolding as a Search Process for Denaturing Sites," *ACS Nano* **10**, 730-738 (2016).
76. L. J. Tauzin, H. Shen, N. A. Moringo, M. H. Roddy, C. A. Bothof, G. W. Griesgraber, A. K. McNulty, J. K. Rasmussen, and C. F. Landes, "Variable surface transport modalities on functionalized nylon films revealed with single molecule spectroscopy," *RSC Advances* **6**, 27760-27766 (2016).

77. B. Shuang, J. Chen, L. Kisley, and C. F. Landes, "Troika of single particle tracking programming: SNR enhancement, particle identification, and mapping," *Phys. Chem. Chem. Phys.* **16**, 624-634 (2014).
78. S. J. Holden, S. Uphoff, and A. N. Kapanidis, "DAOSTORM: an algorithm for high- density super-resolution microscopy," *Nat. Methods* **8**, 279-280 (2011).
79. R. Baraniuk, M. Davenport, R. DeVore, and M. Wakin, "A Simple Proof of the Restricted Isometry Property for Random Matrices," *Constructive Approximation* **28**, 253-263 (2008).
80. M. A. Thompson, M. D. Lew, M. Badieirostami, and W. E. Moerner, "Localizing and Tracking Single Nanoscale Emitters in Three Dimensions with High Spatiotemporal Resolution Using a Double-Helix Point Spread Function," *Nano Lett.* **10**, 211-218 (2010).
81. Y. Hoshino, W. W. Haberaecker, T. Kodama, Z. Zeng, Y. Okahata, and K. J. Shea, "Affinity Purification of Multifunctional Polymer Nanoparticles," *J. Am. Chem. Soc.* **132**, 13648-13650 (2010).
82. Y. Hoshino, M. Nakamoto, and Y. Miura, "Control of Protein-Binding Kinetics on Synthetic Polymer Nanoparticles by Tuning Flexibility and Inducing Conformation Changes of Polymer Chains," *J. Am. Chem. Soc.* **134**, 15209-15212 (2012).
83. Y. Hou, Y. Zhou, H. Wang, R. Wang, J. Yuan, Y. Hu, K. Sheng, J. Feng, S. Yang, and H. Lu, "Macrocyclization of Interferon–Poly(α -amino acid) Conjugates Significantly Improves the Tumor Retention, Penetration, and Antitumor Efficacy," *J. Am. Chem. Soc.* **140**, 1170-1178 (2018).
84. F. Jia, X. Lu, D. Wang, X. Cao, X. Tan, H. Lu, and K. Zhang, "Depth-Profiling the Nuclease Stability and the Gene Silencing Efficacy of Brush-Architected Poly(ethylene glycol)–DNA Conjugates," *J. Am. Chem. Soc.* **139**, 10605-10608 (2017).
85. A. Shundo, K. Hori, T. Ikeda, N. Kimizuka, and K. Tanaka, "Design of a Dynamic Polymer Interface for Chiral Discrimination," *J. Am. Chem. Soc.* **135**, 10282-10285 (2013).
86. M. Jiao, H.-T. Li, J. Chen, A. P. Minton, and Y. Liang, "Attractive Protein-Polymer Interactions Markedly Alter the Effect of Macromolecular Crowding on Protein Association Equilibria," *Biophys. J.* **99**, 914-923 (2010).
87. C. Tan, T. Terakawa, and S. Takada, "Dynamic Coupling among Protein Binding, Sliding, and DNA Bending Revealed by Molecular Dynamics," *J. Am. Chem. Soc.* **138**, 8512-8522 (2016).
88. K. Lindorff-Larsen, N. Trbovic, P. Maragakis, S. Piana, and D. E. Shaw, "Structure and Dynamics of an Unfolded Protein Examined by Molecular Dynamics Simulation," *J. Am. Chem. Soc.* **134**, 3787-3791 (2012).
89. K. Imato, T. Ohishi, M. Nishihara, A. Takahara, and H. Otsuka, "Network Reorganization of Dynamic Covalent Polymer Gels with Exchangeable Diarylbibenzofuranone at Ambient Temperature," *J. Am. Chem. Soc.* **136**, 11839-11845 (2014).

90. T. Cordes, and S. A. Blum, "Opportunities and challenges in single-molecule and single-particle fluorescence microscopy for mechanistic studies of chemical reactions," *Nat. Chem.* **5**, 993-999 (2013).
91. P. Chen, X. Zhou, H. Shen, N. M. Andoy, E. Choudhary, K.-S. Han, G. Liu, and W. Meng, "Single-molecule fluorescence imaging of nanocatalytic processes," *Chem. Soc. Rev.* **39**, 4560-4570 (2010).
92. G. De Cremer, B. F. Sels, D. E. De Vos, J. Hofkens, and M. B. J. Roeffaers, "Fluorescence micro(spectro)scopy as a tool to study catalytic materials in action," *Chem. Soc. Rev.* **39**, 4703-4717 (2010).
93. P. Tinnefeld, and M. Sauer, "Branching Out of Single-Molecule Fluorescence Spectroscopy: Challenges for Chemistry and Influence on Biology," *Angew. Chem. Int. Ed.* **44**, 2642-2671 (2005).
94. Y. He, Y. Li, S. Mukherjee, Y. Wu, H. Yan, and H. P. Lu, "Probing Single-Molecule Enzyme Active-Site Conformational State Intermittent Coherence," *J. Am. Chem. Soc.* **133**, 14389-14395 (2011).
95. L. Kisley, J. Chen, A. P. Mansur, S. Dominguez-Medina, E. Kulla, M. K. Kang, B. Shuang, K. Kourentzi, M.-V. Poongavanam, S. Dhamane, R. C. Willson, and C. F. Landes, "High ionic strength narrows the population of sites participating in protein ion-exchange adsorption: A single-molecule study," *J. Chromatogr. A* **1343**, 135-142 (2014).
96. H. Shen, X. Zhou, N. Zou, and P. Chen, "Single-Molecule Kinetics Reveals a Hidden Surface Reaction Intermediate in Single-Nanoparticle Catalysis," *J. Phys. Chem. C* **118**, 26902-26911 (2014).
97. H. Shen, L. J. Tauzin, R. Baiyasi, W. Wang, N. Moringo, B. Shuang, and C. F. Landes, "Single Particle Tracking: From Theory to Biophysical Applications," *Chem. Rev.* **117**, 7331-7376 (2017).
98. H. Shen, L. J. Tauzin, W. Wang, B. Hoener, B. Shuang, L. Kisley, A. Hoggard, and C. F. Landes, "Single-Molecule Kinetics of Protein Adsorption on Thin Nylon-6,6 Films," *Anal. Chem.* **88**, 9926-9933 (2016).
99. N. A. Moringo, H. Shen, L. J. Tauzin, W. Wang, L. D. C. Bishop, and C. F. Landes, "Variable lysozyme transport dynamics on oxidatively functionalized polystyrene films," *Langmuir* (2017).
100. R. Jungmann, C. Steinhauer, M. Scheible, A. Kuzyk, P. Tinnefeld, and F. C. Simmel, "Single-Molecule Kinetics and Super-Resolution Microscopy by Fluorescence Imaging of Transient Binding on DNA Origami," *Nano Lett.* **10**, 4756-4761 (2010).
101. G. S. Kaminski Schierle, S. van de Linde, M. Erdelyi, E. K. Esbjörner, T. Klein, E. Rees, C. W. Bertoncini, C. M. Dobson, M. Sauer, and C. F. Kaminski, "In Situ Measurements of the Formation and Morphology of Intracellular β -Amyloid Fibrils by Super-Resolution Fluorescence Imaging," *J. Am. Chem. Soc.* **133**, 12902-12905 (2011).
102. X. Michalet, O. Siegmund, J. Vallerga, P. Jelinsky, J. Millaud, and S. Weiss, "Detectors for single-molecule fluorescence imaging and spectroscopy," *J. Mod. Opt.* **54**, 239-281 (2007).

103. E. B. Shera, N. K. Seitzinger, L. M. Davis, R. A. Keller, and S. A. Soper, "Detection of single fluorescent molecules," *Chem. Phys. Lett.* **174**, 553-557 (1990).
104. J. Elf, G.-W. Li, and X. S. Xie, "Probing Transcription Factor Dynamics at the Single-Molecule Level in a Living Cell," *Science* **316**, 1191-1194 (2007).
105. H. Roder, K. Maki, and H. Cheng, "Early Events in Protein Folding Explored by Rapid Mixing Methods," *Chem. Rev.* **106**, 1836-1861 (2006).
106. X. Michalet, S. Weiss, and M. Jäger, "Single-Molecule Fluorescence Studies of Protein Folding and Conformational Dynamics," *Chem. Rev.* **106**, 1785-1813 (2006).
107. J. Tang, Y. Sun, S. Pang, and K. Y. Han, "Spatially encoded fast single-molecule fluorescence spectroscopy with full field-of-view," *Sci. Rep.* **7**, 10945 (2017).
108. V. N Uversky, S. E Permyakov, L. Breydo, E. M Redwan, H. A Almeshdar, and E. A Permyakov, "Disorder in milk proteins: α -Lactalbumin. Part B. A multifunctional whey protein acting as an oligomeric molten globular "oil container" in the anti-tumorigenic drugs, lipotides," *Curr. Protein Pept. Sci.* **17**, 612-628 (2016).
109. Y. Cai, Y. Chen, X. Hong, Z. Liu, and W. Yuan, "Porous microsphere and its applications," *Int. J. Nanomed.* **8**, 1111 (2013).
110. Z. Yang, J. A. Galloway, and H. Yu, "Protein Interactions with Poly(ethylene glycol) Self-Assembled Monolayers on Glass Substrates: Diffusion and Adsorption," *Langmuir* **15**, 8405-8411 (1999).
111. B. Bai, Y. Wu, and R. B. Grigg, "Adsorption and desorption kinetics and equilibrium of calcium lignosulfonate on dolomite porous media," *J. Phys. Chem. C* **113**, 13772-13779 (2009).
112. V. Kiss, and K. Ósz, "Double Exponential Evaluation under Non-Pseudo-First-Order Conditions: A Mixed Second-Order Process Followed by a First-Order Reaction," *Int. J. Chem. Kinet.* **49**, 602-610 (2017).
113. B. P. English, M. Wei, A. M. Van Oijen, K. T. Lee, G. Luo, H. Sun, B. J. Cherayil, S. Kou, and X. S. Xie, "Ever-fluctuating single enzyme molecules: Michaelis-Menten equation revisited," *Nat. Chem. Biol.* **2**, 87 (2006).
114. T. G. Terentyeva, J. Hofkens, T. Komatsuzaki, K. Blank, and C.-B. Li, "Time-resolved single molecule fluorescence spectroscopy of an α -chymotrypsin catalyzed reaction," *J. Phys. Chem. B* **117**, 1252-1260 (2013).
115. S. Myong, M. M. Bruno, A. M. Pyle, and T. Ha, "Spring-Loaded Mechanism of DNA Unwinding by Hepatitis C Virus NS3 Helicase," *Science* **317**, 513-516 (2007).
116. J. I. Steinfeld, J. S. Francisco, and W. L. Hase, *Chemical kinetics and dynamics* (Prentice Hall Englewood Cliffs (New Jersey), 1989).
117. D. L. Floyd, J. R. Ragains, J. J. Skehel, S. C. Harrison, and A. M. van Oijen, "Single-particle kinetics of influenza virus membrane fusion," *Proc. Natl. Acad. Sci. U.S.A.* **105**, 15382-15387 (2008).
118. W. Xu, J. S. Kong, and P. Chen, "Single-Molecule Kinetic Theory of Heterogeneous and Enzyme Catalysis," *J. Phys. Chem. C* **113**, 2393-2404 (2009).
119. H. P. Lu, L. Xun, and X. S. Xie, "Single-Molecule Enzymatic Dynamics," *Science* **282**, 1877-1882 (1998).

120. T. Wei, M. A. Carignano, and I. Szleifer, "Molecular Dynamics Simulation of Lysozyme Adsorption/Desorption on Hydrophobic Surfaces," *J. Phys. Chem. B* **116**, 10189-10194 (2012).
121. T. Hattori, R. Hallberg, and P. L. Dubin, "Roles of Electrostatic Interaction and Polymer Structure in the Binding of β -Lactoglobulin to Anionic Polyelectrolytes: Measurement of Binding Constants by Frontal Analysis Continuous Capillary Electrophoresis," *Langmuir* **16**, 9738-9743 (2000).
122. S. Sakata, Y. Inoue, and K. Ishihara, "Molecular Interaction Forces Generated during Protein Adsorption to Well-Defined Polymer Brush Surfaces," *Langmuir* **31**, 3108-3114 (2015).
123. A. C. McUmbler, T. W. Randolph, and D. K. Schwartz, "Electrostatic Interactions Influence Protein Adsorption (but Not Desorption) at the Silica-Aqueous Interface," *J. Phys. Chem. Lett.* **6**, 2583-2587 (2015).
124. A. C. Dumetz, A. M. Snellinger-O'Brien, E. W. Kaler, and A. M. Lenhoff, "Patterns of protein-protein interactions in salt solutions and implications for protein crystallization," *Protein Sci.* **16**, 1867-1877 (2007).
125. X. Zhang, and R. Bai, "Adsorption behavior of humic acid onto polypyrrole-coated nylon 6,6 granules," *J. Mater. Chem.* **12**, 2733-2739 (2002).
126. C. Bramaud, P. Aimar, and G. Daufin, "Whey protein fractionation: Isoelectric precipitation of α -lactalbumin under gentle heat treatment," *Biotechnol. Bioeng.* **56**, 391-397 (1997).
127. N. J. Greenfield, "Using circular dichroism spectra to estimate protein secondary structure," *Nat. Protoc.* **1**, 2876 (2006).
128. A. Micsonai, F. Wien, L. Kernya, Y.-H. Lee, Y. Goto, M. Réfrégiers, and J. Kardos, "Accurate secondary structure prediction and fold recognition for circular dichroism spectroscopy," *Proc. Natl. Acad. Sci. U.S.A.* **112**, E3095-E3103 (2015).
129. M. Svensson, H. Sabharwal, A. Håkansson, A.-K. Mossberg, P. Lipniunas, H. Leffler, C. Svanborg, and S. Linse, "Molecular Characterization of α -Lactalbumin Folding Variants That Induce Apoptosis in Tumor Cells," *J. Biol. Chem.* **274**, 6388-6396 (1999).
130. C. Nishimura, V. N. Uversky, and A. L. Fink, "Effect of Salts on the Stability and Folding of Staphylococcal Nuclease," *Biochemistry* **40**, 2113-2128 (2001).
131. C. Toniolo, A. Polese, F. Formaggio, M. Crisma, and J. Kamphuis, "Circular Dichroism Spectrum of a Peptide 310-Helix," *J. Am. Chem. Soc.* **118**, 2744-2745 (1996).
132. S. M. Kelly, T. J. Jess, and N. C. Price, "How to study proteins by circular dichroism," *BBA - Proteins and Proteomics* **1751**, 119-139 (2005).
133. K. C. Dee, D. A. Puleo, and R. Bizios, "An introduction to tissue-biomaterial interactions," *Cell Mol. Biol.* **8**, 419-425 (2004).
134. N. Yu, P. Genevet, M. A. Kats, F. Aieta, J.-P. Tetienne, F. Capasso, and Z. Gaburro, "Light propagation with phase discontinuities: generalized laws of reflection and refraction," *Science* **334**, 333-337 (2011).

135. X. Ni, N. K. Emani, A. V. Kildishev, A. Boltasseva, and V. M. Shalaev, "Broadband light bending with plasmonic nanoantennas," *Science* **335**, 427-427 (2012).
136. H. Sasaki, K. Yamamoto, Y. Ichihashi, and T. Senoh, "Image Size Scalable Full-parallax Coloured Three-dimensional Video by Electronic Holography," *Sci. Rep.* **4**, 4000 (2014).
137. S. Yamada, T. Kakue, T. Shimobaba, and T. Ito, "Interactive Holographic Display Based on Finger Gestures," *Sci. Rep.* **8**, 2010 (2018).
138. E. R. Dowski, and W. T. Cathey, "Extended depth of field through wave-front coding," *Appl. Opt.* **34**, 1859-1866 (1995).
139. S. Bagheri, and B. Javidi, "Extension of depth of field using amplitude and phase modulation of the pupil function," *Opt. Lett.* **33**, 757-759 (2008).
140. R. E. Thompson, D. R. Larson, and W. W. Webb, "Precise Nanometer Localization Analysis for Individual Fluorescent Probes," *Biophys. J.* **82**, 2775-2783 (2002).
141. S. R. Pavani, and R. Piestun, "High-efficiency rotating point spread functions," *Opt Express* **16**, 3484-3489 (2008).
142. W. E. Moerner, Y. Shechtman, and Q. Wang, "Single-molecule spectroscopy and imaging over the decades," *Faraday Discussions* **184**, 9-36 (2015).
143. M. Badieirostami, M. D. Lew, M. A. Thompson, and W. Moerner, "Three-dimensional localization precision of the double-helix point spread function versus astigmatism and biplane," *Applied physics letters* **97**, 161103 (2010).
144. M. D. Lew, S. F. Lee, M. Badieirostami, and W. E. Moerner, "Corkscrew point spread function for far-field three-dimensional nanoscale localization of pointlike objects," *Optics Letters* **36**, 202-204 (2011).
145. Y. Shechtman, L. E. Weiss, A. S. Backer, S. J. Sahl, and W. E. Moerner, "Precise Three-Dimensional Scan-Free Multiple-Particle Tracking over Large Axial Ranges with Tetrapod Point Spread Functions," *Nano Lett* **15**, 4194-4199 (2015).
146. N. A. Moringo, H. Shen, L. D. C. Bishop, W. Wang, and C. F. Landes, "Enhancing Analytical Separations Using Super-Resolution Microscopy," *Annual Review of Physical Chemistry* **69**, 353-375 (2018).
147. M. A. Thompson, J. M. Casolari, M. Badieirostami, P. O. Brown, and W. E. Moerner, "Three-dimensional tracking of single mRNA particles in *Saccharomyces cerevisiae* using a double-helix point spread function," *Proceedings of the National Academy of Sciences* **107**, 17864-17871 (2010).
148. V. Sundaresan, K. Marchuk, Y. Yu, E. J. Titus, A. J. Wilson, C. M. Armstrong, B. Zhang, and K. A. Willets, "Visualizing and Calculating Tip-Substrate Distance in Nanoscale Scanning Electrochemical Microscopy Using 3-Dimensional Super-Resolution Optical Imaging," *Anal. Chem.* **89**, 922-928 (2017).
149. W. Wang, H. Shen, N. A. Moringo, N. C. Carrejo, F. Ye, J. T. Robinson, and C. F. Landes, "Super-Temporal-Resolved Microscopy Reveals Multistep Desorption Kinetics of α -Lactalbumin from Nylon," *Langmuir* **34**, 6697-6702 (2018).
150. J. R. Fienup, "Phase retrieval algorithms: a comparison," *Appl. Opt.* **21**, 2758-2769 (1982).

151. Y. Shechtman, S. J. Sahl, A. S. Backer, and W. E. Moerner, "Optimal point spread function design for 3D imaging," *Phys Rev Lett* **113**, 133902 (2014).
152. P. N. Petrov, Y. Shechtman, and W. E. Moerner, "Measurement-based estimation of global pupil functions in 3D localization microscopy," *Opt. Express* **25**, 7945-7959 (2017).
153. H. H. Bauschke, P. L. Combettes, and D. R. Luke, "Phase retrieval, error reduction algorithm, and Fienup variants: a view from convex optimization," *J. Opt. Soc. Am. A* **19**, 1334-1345 (2002).
154. J. R. Fienup, and C. C. Wackerman, "Phase-retrieval stagnation problems and solutions," *J. Opt. Soc. Am. A* **3**, 1897-1907 (1986).
155. Å. Björck, *Numerical Methods for Least Squares Problems*.
156. L. Bottou, "Large-scale machine learning with stochastic gradient descent," in *Proceedings of COMPSTAT'2010*(Springer, 2010), pp. 177-186.
157. B. Recht, C. Re, S. Wright, and F. Niu, "Hogwild: A lock-free approach to parallelizing stochastic gradient descent," in *Advances in neural information processing systems*(2011), pp. 693-701.
158. G. Grover, K. DeLuca, S. Quirin, J. DeLuca, and R. Piestun, "Super-resolution photon-efficient imaging by nanometric double-helix point spread function localization of emitters (SPINDLE)," *Opt. Express* **20**, 26681-26695 (2012).
159. A. Rammohan, P. K. Dwivedi, R. Martinez-Duarte, H. Katepalli, M. J. Madou, and A. Sharma, "One-step maskless grayscale lithography for the fabrication of 3-dimensional structures in SU-8," *Sensors and Actuators B: Chemical* **153**, 125-134 (2011).
160. W. Wang, H. Shen, N. A. Moringo, N. C. Carrejo, F. Ye, J. T. Robinson, and C. F. Landes, "Super-temporal resolved microscopy reveals multistep desorption kinetics of α -lactalbumin from nylon," *Langmuir* (2018).
161. L. Zhu, W. Zhang, D. Elnatan, and B. Huang, "Faster STORM using compressed sensing," *Nature Methods* **9**, 721 (2012).